A Spectral Approach to Noninvasive Model-Based Estimation of Intracranial Pressure

by

James Noraky

S.B., Massachusetts Institute of Technology (2013)

Submitted to the Department of Electrical Engineering and Computer Science
in Partial Fulfillment of the Requirements for the Degree of

Master of Engineering in Electrical Engineering and Computer Science

at the

MASSACHUSETTS INSTITUTE OF TECHNOLOGY

June 2014

Signature redacted

Author ....
Department of Electrical Engineering and Computer Science
May 21, 2014

Signature redacted

Certified by ....
Thomas Heldt
Hermann L.F. von Helmholtz Career Development Assistant Professor
Thesis Supervisor

Signature redacted

Accepted by ....
Albert R. Meyer
Chairman, Masters of Engineering Thesis Committee

A Spectral Approach to Noninvasive Model-Based Estimation of Intracranial Pressure

by

James Noraky

Submitted to the Department of Electrical Engineering and Computer Science

May 21, 2014

In Partial Fulfillment of the Requirements for the Degree of Master of Engineering

in Electrical Engineering and Computer Science

Abstract

Intracranial pressure (ICP) is the hydrostatic pressure of the cerebrospinal fluid. Ideally, ICP should be monitored in many neuropathological conditions, as elevated ICP is correlated with poor neurocognitive outcomes after injuries to the brain. Measuring ICP requires the surgical placement of a sensor or catheter into the brain tissue or cerebrospinal fluid spaces of the brain. With the risk of infection and brain damage, ICP is only measured in a small subset of those patients whose treatment could benefit from knowing ICP. We expand on a previously proposed model-based time-domain approach to noninvasive, patient-specific and continuous estimation of ICP using routinely measured waveforms that has been validated on patients with traumatic brain injuries. Here, we present a model-based algorithm to estimate ICP using the functional relationship between the spectral densities of the routinely measured waveforms. We applied this algorithm to both a simulated and clinical dataset. For the simulated dataset, we achieved a mean error (bias) of 1.2 mmHg and a standard deviation of error (SDE) of 2.2 mmHg. For the clinical dataset of patients with traumatic brain injuries, we achieved a bias of 13.7 mmHg and a SDE of 15.0 mmHg. While the clinical results are not favorable, we describe sources of estimation error and future directions of research to improve the ICP estimates.

Acknowledgments

I owe an enormous debt of gratitude to Professors **Thomas Heldt** and **George Verghese** who have been excellent mentors in guiding me through my research. Under their mentorship, they have shown me the importance of dwelling on a problem to avoid overlooking the nuances and details that are essential to understanding the problem. I am also grateful to both Thomas and George for instilling in me the importance of documentation, an area where I am weak. In drafting and revising this document, I have managed to consolidate my thoughts and gain a sense of clarity in my mind. Needless to say, I will remember these important research lessons throughout my entire career. I have known both George and Thomas for most of my time here at MIT, both as an undergraduate and now as a graduate student, and words simply cannot capture how supportive and encouraging they have been to me. They have made my experience thus far intellectually stimulating and fun.

I also express my gratitude to **Andrea Fanelli** who has been a very helpful sounding board for my research ideas. I also thank my wonderful friends who have made graduate school extremely enjoyable: **Orhan Celiker**, **Hoon Cho**, **Rui Jin**, **Albert Kim**, and **Haoyang Zeng**, who all share my love for deep-fried chicken; **Fabian Kozynski**, **Anuran Makur**, and **Lucas Nissenbaum**, who provided helpful comedic relief throughout this process. Finally, I thank my mother, sister, and grandparents for supporting me throughout every stage of my education.

Contents

List of Figures

Chapter 1

Introduction

Intracranial pressure (ICP) is the hydrostatic pressure of the cerebrospinal fluid. In healthy supine adults, ICP ranges from 7 mmHg to 15 mmHg [20]. When the brain is injured, ICP may rise and if left untreated, the patient's prognosis worsens. In this chapter, we discuss the importance of ICP in directing therapies for injuries to and diseases that affect the brain. We follow this discussion with a survey of the current measurement modalities used to monitor ICP. We argue that these measurement modalities are insufficient, as they are used in only a small subset of those patients who could potentially benefit from knowing ICP. We then describe noninvasive approaches towards ICP estimation. We describe our contribution to this field of investigation and provide an overview of this thesis.

1.1 The Importance of Intracranial Pressure

ICP is an important vital sign of the brain, as elevated ICP has been shown to correlate with poor outcome in patients with brain injuries. In this section, we discuss neurological diseases in which knowledge of ICP is critical. If undetected, elevated ICP can lead to cerebral ischema, which is reduced oxygen delivery to the brain, resulting in brain damage. In extreme cases, elevated ICP can even lead to brain herniation and death [20]. Here, we will describe the neuropathologies for which knowledge of ICP is essential: hemorrhagic stroke, hydrocephalus, and traumatic brain injury.

1.1.1 Hemorrhagic Strokes

Stroke is the fourth leading cause of death in the United States [3]. A stroke occurs when blood flow to the brain is reduced. Strokes can be further categorized into ischemic and hemorrhagic types. The most common type, ischemic stroke, is caused by obstruction of blood flow in the arteries that supply blood to the brain. Hemorrhagic strokes are caused by bleeding within the cranial cavity due to either forceful means (e.g. trauma to the head) or through non-forceful means (e.g. brain aneurysms). While hemorrhagic strokes account for only 15% of all strokes, the associated mortality rate is higher than that of ischemic strokes [17]. Here, we focus our attention on hemorrhagic strokes and their effect on ICP.

Hemorrhagic strokes are categorized into extra-axial hemorrhages and intra-axial hemorrhage. An extra-axial hemorrhage is a bleed within the skull, but outside the brain tissue whereas intra-axial hemorrhage occurs within the brain tissue. Examples of extra-axial hemorrhage include epidural, subdural, and subarachnoid hemorrhages. Examples of intra-axial hemorrhage include intraparenchymal and intraventricular hemorrhages [3]. The bleeding within or around the brain leads to localized accumulation of blood (hematomas) outside of blood vessels [22]. Due to the fixed volume of the skull, this additional accumulation of volume results in an increase in ICP. Consequently, clinicians monitor ICP in these patients. When ICP exceeds 20 mmHg, aggressive therapy is started to reduce ICP [17].

1.1.2 Hydrocephalus

Hydrocephalus is an abnormal accumulation of cerebrospinal fluid (CSF) through an imbalance between the generation and reabsorption of CSF. Hydrocephalus can be caused by injury to the brain and can occur in infants. Hydrocephalus is estimated to affect 1.5 million individuals in the US. Furthermore, hydrocephalus is also one of the most common birth defects [1].

Hydrocephalus is classified into communicating and non-communicating forms. In communicating hydrocephalus, the reabsorption of cerebrospinal fluid is impaired, whereas in non-communicating hydrocephalus, obstructions prevent the circulation of cerebrospinal fluid thereby causing localized accumulation [1]. Similar to hematomas, the accumulation of CSF compresses brain tissue and increases ICP. To prevent ischemia and brain herniation, clinicians monitor ICP and begin ICP lowering therapy when its value exceeds 15 mmHg [20].

1.1.3 Traumatic Brain Injuries

Traumatic brain injuries (TBI) are caused by external forces applied the head that damage the internal structure of the brain. If left untreated, TBI can result in impaired cognitive function, depression, and death [4]. TBIs are common and can be caused by accidents, sport injuries, and physical assault. In 2010, there were 2.5 million cases of TBIs, and collectively, TBIs represent 30% of all injury deaths in the US [4]. Due to the force of the blunt trauma, localized accumulation of interstitial fluids (edemas) can form in the brain, leading to an increase in ICP. For patients hospitalized with severe TBI, ICP is generally monitored and maintained to be less than 20 mmHg [20].

Given the importance of ICP in managing a variety of injuries, we describe next the current measurement modalities used to measure ICP.

1.2 Current Measurement Modalities

In the previous section, we described the importance of ICP in directing therapies for different neurological diseases. The modalities we describe below are highly invasive as they require a neurosurgeon to drill a hole in the skull and insert a sensor or catheter into the brain tissue or the CSF space. Figure 1.1 summarizes the different ways in which ICP can be monitored.

The clinical gold standard for measuring ICP involves the surgical placement of a catheter into the ventricular spaces of the brain. This approach is used in severe TBI, given the high risk of infection (11%) and brain damage [20]. It is also used in subarachnoid hemorrhages and hydrocephalus, for example, if CSF needs to be drained. As an alternative to ventricular measurements, ICP can also be measured by sensors placed in the brain parenchymal spaces. While this procedure carries less risk of infection, these solid-state sensors have a tendency to exhibit baseline wander. Furthermore, once implanted, these sensors cannot be recalibrated [20]. An analysis of the accuracy of a Codman intraparenchymal probe reveals an absolute error of 6 mmHg when compared to ventricular measurements [19].

ICP can also be measured by surgically placing sensors into the subarachnoid, subdural, and epidural spaces of the brain. The benefit of these approaches is the fact that there is less risk of brain infection, but these techniques have fallen out of favor due to the lack of reliability [20]. ICP measured by these probes can differ by at much as 10 mmHg or more when compared to intraparenchymal probes [10].

Given the invasive nature of these measurement modalities and the associated risks, ICP is only measured and utilized in a small subset of brain pathologies, typically those deemed severe. In mild forms of hydrocephalus and TBI, for example, ICP might still be very important to monitor to avoid undesirable side effects. The limitation of these measurement modalities motivates the development of noninvasive approaches to estimate intracranial pressure. In the next section, we describe those approaches.

1.3 Approaches to Estimating Intracranial Pressure

Ideally, we require approaches to ICP estimation to be minimally or non-invasive and to allow for continuous and accurate monitoring. In most of the algorithms described below, arterial blood pressure (ABP) and cerebral blood flow velocity (CBFV) are used to estimate ICP [15]. Both of these signals can be continuously

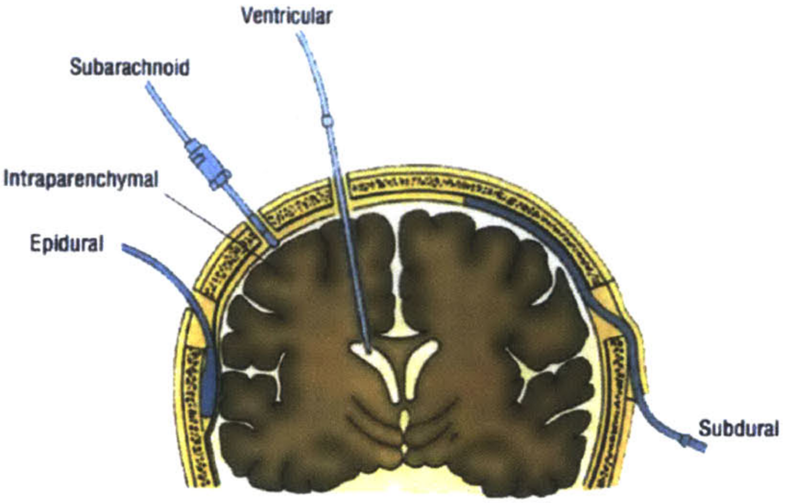

Figure 1.1: The different locations for the placement of catheters and sensors used to measure ICP. Figure adapted from [12].

measured in a non- or minimally invasive fashion. The techniques we summarize come in two flavors. The "black-box" approaches to ICP estimation exploits patterns and statistical associations in related physiological data streams to estimate ICP. The "physiology-motivated" approaches utilize physiological insights to estimate ICP. For a relatively recent review of noninvasive ICP estimation approaches, see [10]. First, we describe the black-box estimators.

1.3.1 Black-Box Approaches

In [18], Schmidt *et al.* applies a filter to the ABP waveform to estimate ICP. In this approach, features in the ABP and CBFV waveform are used to estimate the filter coefficients. This approach was initially validated on 11 patients with a bias of 3.8 mmHg and a standard deviation of error (SDE) of 1.9 mmHg.

A similar methodology is presented in [8]. In this approach, Hu *et al.* associate a transfer function with ABP, CBFV, and ICP within a training set. To estimate ICP, the algorithm takes as input ABP and CBFV and estimates ICP by applying the transfer function that is chosen based on features of the input signals. However, the authors provides no clear metrics to quantify the performance of this approach.

In [6], Chacon *et al.* used kernel methods to design regression based estimators to estimate ICP. The authors extract features from ABP and CBFV and then train estimators using radial basis kernels to estimate the corresponding value of ICP. This approach was validated on 8 patients with a bias of 0.15 mmHg and a SDE of 1.8 mmHg.

While the performance statistics look very promising, they have been obtained on very small sample sizes of patients and it remains to be seen when they hold up for larger populations with heterogeneous pathologies.

In all of these approaches, a training set is required to generate the estimators. Because ICP is estimated using the features of ABP and CBFV, estimators must also be trained for different pathologies. Developing black-box algorithms also require consistent measurements. While ABP can be consistently measured, CBFV cannot. Depending on the angle of insonation in which the CBFV is measured, the amplitude of the signal can vary. Given the need for large datasets and the intrinsic difficulty of measuring reproducible CBFV waveforms, these black-box approaches are generally unreliable. In the next section, we describe another category of algorithms that exploits physiological knowledge to estimate ICP.

1.3.2 Physiology-Motivated Approaches

We describe physiology-motivated algorithms to estimate ICP. These approaches are based on the premise that changes in ICP can be inferred from appropriate measurements and an understanding of the underlying physiology. Furthermore, unlike the black-box approaches, these techniques do not require a training set.

In [16], Rauguskus *et al.* exploit the relevant physiology of the central retinal artery. The authors realize that the intracranial segment of the central retinal artery is compressed by ICP whereas the extracranial segment is compressed by intraocular pressure. When the two pressures are equal, the morphology of the CBFV waveform should be the same in both the intracranial and extracranial artery. This balance is achieved by applying an external pressure to the eye until certain measures of the CBFV morphology are the same in the two segments as confirmed by a two-depth transcranial Doppler sonar. This applied pressure is taken to be ICP. Ragauskus validated this approach on 62 patients and achieved a bias of 0.12 mmHg and a SDE of 2.19 mmHg. Given the measurement modality, however, this is not a feasible method for continuous ICP monitoring due to the need for applying continuous pressure to the eye.

In [11], Kashif *et al.* exploit the role ICP plays in the cerebral circulation and use a parameterized model of the cerebrovascular system to estimate ICP. This algorithm takes as inputs, windowed segments of ABP and CBFV waveforms, and outputs estimates of cerebrovascular compliance, cerebrovascular resistance, and mean ICP for each estimation window. This approach has been validated on 37 patients with traumatic brain injuries with a bias of 1.5 mmHg and a SDE of 5.9 mmHg. These performance statistics are comparable to certain invasive ICP measurement modalities. In this thesis, we extend the work of Kashif by addressing the limitations of the approach and developing a new algorithm to estimate ICP. In the next section, we outline the organization of this thesis.

1.4 Organization of the Thesis

In the next chapter, we will provide an overview of the relevant physiology of the cerebrovascular system and the mathematical models used to represent it. We also will describe the Kashif algorithm and discuss the limitations of the approach.

In Chapter 3, we introduce two algorithms for ICP estimation. First, we will describe a heuristic to address a limitation of the Kashif algorithm. Then, we develop and reformulate an algorithm for ICP estimation using the spectral density of the input time-series. We refer to these approaches as the time-domain (TD) and spectral-density (SD) algorithms, respectively.

In Chapter 4, we apply both the TD and SD algorithms to simulated data and real patient datasets. We compare the results of applying these algorithms to both dataset and discuss the limitations of both approaches.

In Chapter 5, we summarize our work and discuss future avenues of research.

Chapter 2

Background

In this chapter, we present an overview of the work that motivated the development of the algorithms for intracranial pressure (ICP) estimation. First, we provide a review of the relevant anatomy and physiology of the cerebrovascular system. Then, we discuss different mathematical models used to represent the dynamics of blood flow within the brain's vasculature and how they are used. We conclude with a description of a recent model-based approach to estimate ICP, which inspired the development of two algorithms presented in the following chapter.

2.1 Relevant Physiology

The cerebrovascular system is comprised of a network of blood vessels through which the brain is supplied with oxygen- and nutrient-rich blood, and carbon dioxide and other metabolic waste are removed. Here, we will describe the arterial and venous systems of the cerebral vasculature, as well as the anatomy of the cerebrospinal fluid spaces. Understanding the fluid interactions within these systems will allow us later to develop mathematical models from which variables like ICP can be estimated.

2.1.1 Arterial and Venous System

Blood enters the cerebrovascular system through the paired common carotid and vertebral arteries. The latter set of arteries join to form the single basilar artery. The basilar artery and internal carotids in turn join to form an interconnection known as the Circle of Willis, from which the paired anterior cerebral, middle cerebral, and posterior cerebral arteries branch off and supply blood to both hemispheres of the brain [9]. The anatomy of the large cerebral arteries is shown in Figure 2.1A.

Gas and nutrient exchange occur at the level of the cerebral microcirculation. Downstream of these

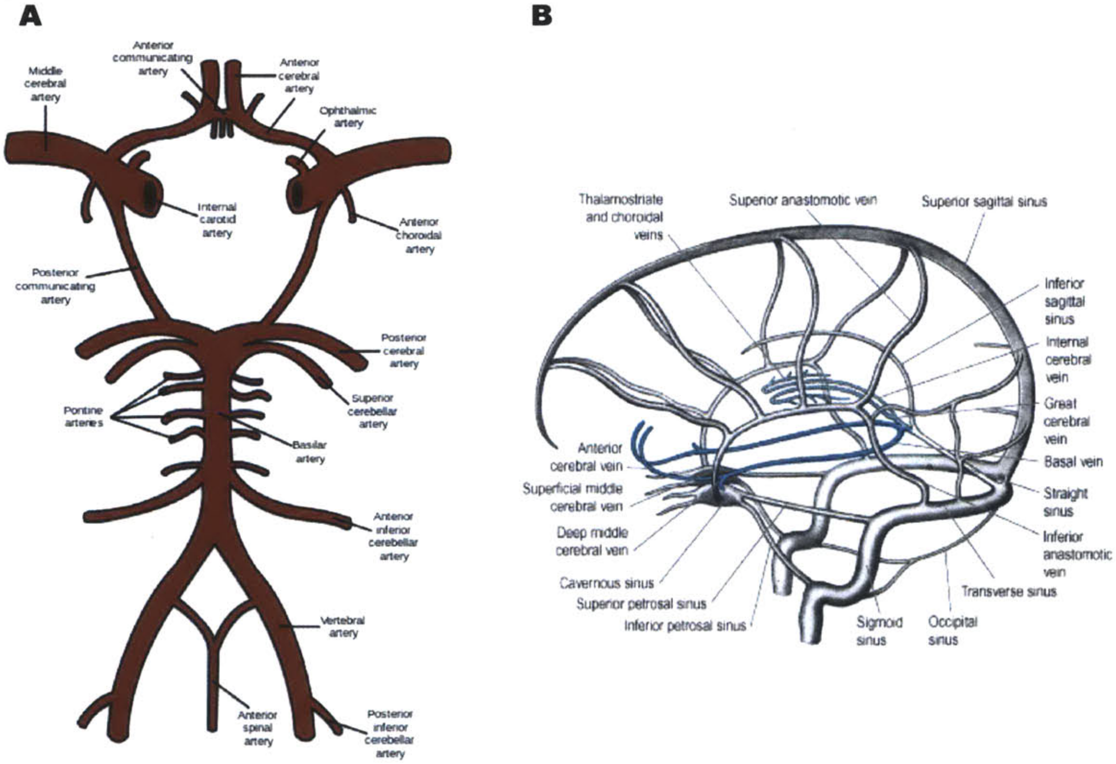

Figure 2.1: (A) The main arteries of the brain. (B) The venous system of the brain. Figure adapted from [2].

capillary networks, the oxygen- and nutrient-depleted blood is collected in the venous system, through a network of venules and veins. The veins located on the surface of the brain form the superficial system, which includes the large superior sagittal sinus. The veins within the brain form the deep system and merge into the Great cerebral vein (of Galen). Both of these systems join at the confluence of sinuses, allowing blood to flow into the jugular veins. Figure 2.1B illustrates the venous system in the brain.

Adequate blood flow is vital to brain function. On average, blood flow through the brain occurs at 750 ml/min, or 18-20% of cardiac output [9]. Insufficient blood flow to the brain is known as cerebral ischemia. If ischemia is allowed to continue for a few minutes, brain tissue becomes damaged and eventually dies. If there is too much blood flow, a condition known as hyperemia, the volume of the arteries can increase to the point where brain tissue is compressed. To maintain adequate flow, a mechanism known as autoregulation affects the properties of the cerebrovascular circulation by dilating or constricting the arteries and arterioles in response to local metabolic demand or changes in perfusion pressure.

2.1.2 Cerebrospinal Fluid

The brain is surrounded by cerebrospinal fluid (CSF) that provides mechanical support and protection for the brain tissue. CSF is a filtrate that is secreted from specialized networks of the cerebrovascular microcirculation (the choroid plexus) located in the four chambers (ventricles) of the brain. The capillaries are sheathed in a layer of epithelial cells that form the the blood-brain barrier, and generate CSF by filtering plasma through active transport mechanisms. The production of CSF is on average 500 ml per day [9]. The CSF then flows from the ventricles through aqueducts into the cisterns, subarachnoid space, and sulci of the brain. From the subarachnoid space, the CSF is reabsorbed into the venous system through protrusions (arachnoid villi) into the superficial system of the cerebral veins. On average, CSF is turned over three to four times per day [9]. The generation and circulation of CSF is shown in Figure 2.2.

The hydrostatic pressure of the CSF is termed the ICP. Rather than venous pressure, ICP serves as the downstream pressure for cerebral perfusion due to the distensibility of the cerebral venules. The venules in the subarachnoid space are immersed in CSF, and when ICP exceeds venous pressure, the venules exhibit collapsible flow. Since venous pressure normally ranges from 4-6 mmHg and ICP normally ranges from 7-15 mmHg, flow in the cerebral veins is collapsible [20]. Hence, cerebral perfusion pressure (CPP) is the pressure difference between arterial pressure and ICP.

In the next section, we discuss the development of mathematical models of the cerebrovascular physiology that relate arterial pressure, ICP, and cerebral blood flow.

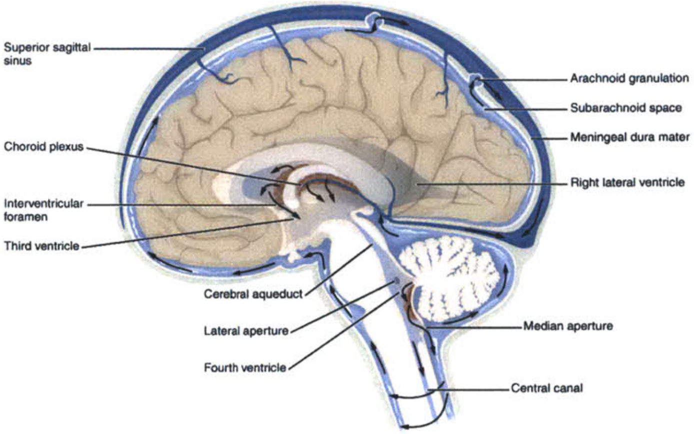

Figure 2.2: The generation and circulation of CSF in the ventricular system. Figure adapted from [2].

2.2 Models of the Cerebrovascular System

Here, we examine mathematical, mechanistic models of the cerebrovascular system that relate CPP to cerebral blood flow (CBF). We focus on models that incorporate the descriptions of the arterial, venous, and ventricular system of the cerebral vasculature. Here, we describe three models of the cerebrovascular system and discuss the ways in which they are used.

2.2.1 Ursino-Lodi Model

The Ursino-Lodi model [21] of the cerebrovascular system is shown in Figure 2.3. The model is a circuit abstraction of the dynamics between the CBF and CPP.

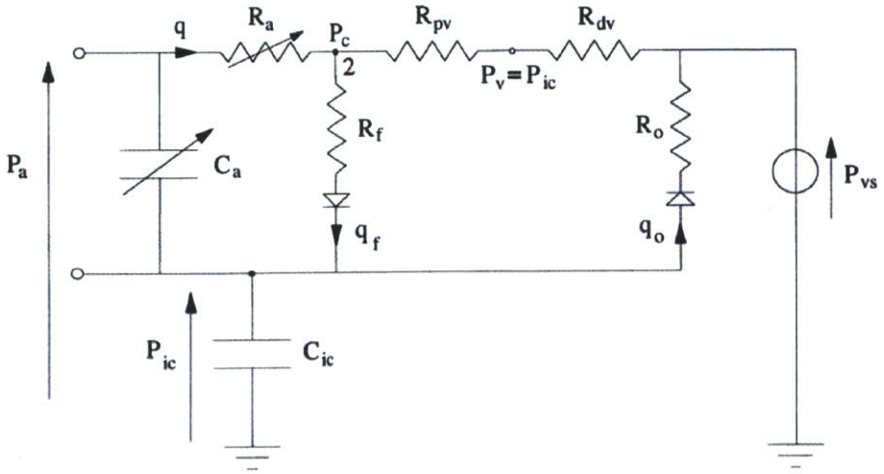

Figure 2.3: Ursino-Lodi model of the cerebrovascular system. Figure adapted from [21].

The model relates ABP to CBF, denoted as P_a and q, respectively, through a network that compartmentalizes the different subsystems of the cerebrovascular system. The autoregulatory nature of the arterial system is represented by the variable resistor R_a and capacitor C_a, respectively; the secretion of CSF from the choroid plexus into the ventricular spaces is captured by the current q_f, through the resistor R_f; the venous system is represented by the resistors R_{pv} and R_{dv}, where the collapsible flow is enforced by the relation $P_v = P_{ic}$; finally, the reabsorption of CSF into the superficial subsystem is represented by the current q_o, through the resistor R_o. In this model, ICP is determined by the charge on the capacitor C_{ic} [21].Ursino *et al.* used the model to simulate the dynamics of mean ICP on a beat-by-beat basis. The authors found that with a physiologically motivated choice of parameters and measurements of ABP and CBF, the trends and dynamics of the simulated ICP resembled real measurements observed in clinical settings.

We consider two natural extensions of this model: (1) using it to simulate the pulsatility of the waveforms in the cerebrovascular system and (2) using it to estimate ICP. To accomplish both, we describe simplified models of the cerebrovascular system inspired by the Ursino-Lodi model. We begin with a description of a model that can be used to simulate pulsatile waveforms.

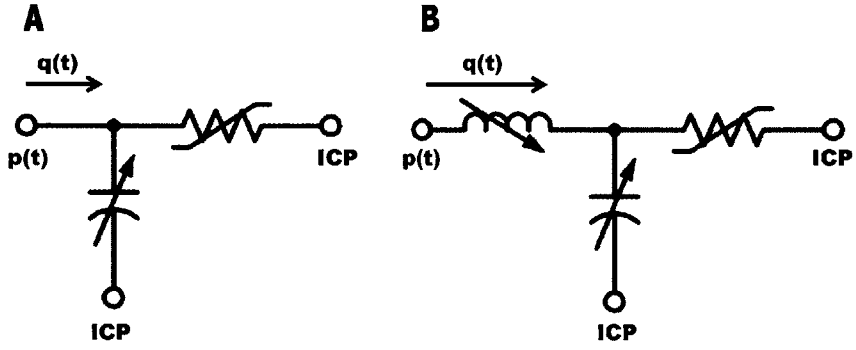

Figure 2.4: (A) Kashif model of the cerebrovascular system. Adapted from [11]. (B) Inductive model of the cerebrovascular system.

2.2.2 Inductive Model

We present a simplified model that can be used to simulate pulsatile waveforms in the cerebrovascular system. This model was developed based on the following insights: (1) the generation and the reabsorption of CSF are much slower than the perfusion of blood through the brain and (2) the mass of the blood restricts instantaneous changes in blood flow. Using the first insight, we see that R_f and R_o in the Ursino-Lodi model can be approximated as open circuits over short durations. We combine the remaining resistors and capacitors and add an inductor to capture the inertial properties of blood, thereby accounting for the second insight. The reduced model of the cerebrovascular system is shown in Figure 2.4B.

We can describe this model with the following second-order differential equation

$$q(t)+\frac{L}{R}\frac{dq(t)}{dt}+LC\frac{d^2q(t)}{dt^2} = \frac{p(t)-p_{ICP}(t)}{R}+C\frac{d(p(t)-p_{ICP}(t))}{dt} \tag{2.1}$$

where we denote $q(t)$, $p(t)$, $p_{ICP}(t)$ as the CBF, ABP, and ICP waveforms, respectively; and R, L, and C are the aggregate resistance, inductance, and capacitance of the cerebral vasculature.

To simulate CBF, we use ABP and ICP waveforms, sampled at a nominal sampling frequency f_S. For the ease of computation, we will simulate the CBF waveform in a stage-wise fashion. This motivates rewriting (2.1) in the following manner

$$y(t)=\frac{p(t)-p_{ICP}(t)}{R}+C\frac{d(p(t)-p_{ICP}(t))}{dt} \tag{2.2}$$

$$y(t)=q(t)+\frac{L}{R}\frac{dq(t)}{dt}+LC\frac{d^2q(t)}{dt^2} \tag{2.3}$$

Furthermore, we also rewrite (2.3) in the standard state-space representation as follows. Let $z(t) = \left(\frac{dq(t)}{dt}, q(t)\right)^T$, we then have

$$\dot{z}(t)=\begin{bmatrix} -\frac{1}{LC} & -\frac{1}{RC} \\ 1 & 0 \end{bmatrix} z(t)+\begin{bmatrix} \frac{1}{LC} \\ 0 \end{bmatrix} y(t) \tag{2.4}$$

$$q(t)=\begin{bmatrix} 0 & 1 \end{bmatrix} z(t)+0\cdot y(t) \tag{2.5}$$

We define

$$A=\begin{bmatrix} -\frac{1}{LC} & -\frac{1}{RC} \\ 1 & 0 \end{bmatrix}$$

$$B=\begin{bmatrix} \frac{1}{LC} \\ 0 \end{bmatrix}$$

$$C=\begin{bmatrix} 0 \\ 1 \end{bmatrix}^T$$

$$D=0$$

Denoting the time-sampled ABP and ICP waveforms as $p[n]$ and $x[n]$, respectively, we first discretize (2.2) as follows

$$y[n] = \frac{p[n] - p_{ICP}[n]}{R} + \frac{Cf_S}{2}(p[n-1] + p[n+1] - 2p[n] - p_{ICP}[n-1] - p_{ICP}[n+1] + 2p_{ICP}[n]) \tag{2.6}$$

where $y[n]$ corresponds to the discretized $y(t)$. Here, we approximate the differentiation in (2.2) as the average between the forward and backward differences.

We then use $y[n]$ as an input to (2.4).We discretize (2.4) and (2.5) as follows

$$z[n+1] = A_d z[n] + B_d y_u[n] \tag{2.7}$$

$$q_u[n] = C_d z[n] + D_d y_u[n] \tag{2.8}$$

where $A_d = e^{\frac{A}{fs}}$; $B_d = A^{-1}(A_d - I)B$, and I is the identity matrix; $C_d = C$; and $D_d = D$. We derive the discretization of the state space representation in Appendix A.

Finally, we simulate CBF, $q[n]$, by iterating through (2.7) and (2.8). (To obtain CBF velocity, we scale $q[n]$ by $\beta \in (0,1]$, assuming a multiplicative relationship between the two signals.)

Using the protocol above, we simulated CBFV waveforms using clinical measurements of ABP and ICP with fixed values of R, L, and C . We implemented the simulation code in Matlab. In our experiments, we observed that with $R \in [0.8, 1.2]$ $\frac{\mathrm{ml}}{\mathrm{sec}\cdot\mathrm{mmHg}}$, $L \in [0.01, 0.1]$ $\frac{\mathrm{mmHg}}{\mathrm{ml/sec}}$, and $C \in [0.01, 0.05]$ $\frac{\mathrm{ml}}{\mathrm{mmHg}}$, the simulated CBF waveforms assume realistic mean values and ranges.

Here, we provide examples of the variety of different simulated waveforms we obtained using one clinical record of ABP and ICP waveforms. Figure 2.5 shows three examples of the simulated CBF waveforms, each generated using different values of R, with L and C held constant. As we increase R, we observe that the mean value of the CBF waveform and the peak-to-peak amplitude both decrease. This is expected since we impose a pressure waveform. As R increases, the flow through the resistor decreases.

Figure 2.6 shows three examples of the simulated CBF waveforms, each generated for different values of L, with R and C held constant. As we increase L, we observe a reduction in the peak height, a widening of the pulse width, and a slower signal transition. This corresponds to a reduction of the high frequency components of the CBF waveform, which is characteristic of an inductive element.

Figure 2.7 shows three examples of the simulated CBF waveforms, each generated using different values of C, with R and L held constant. As we increase C, we observe an increase in the peak height, a shortening

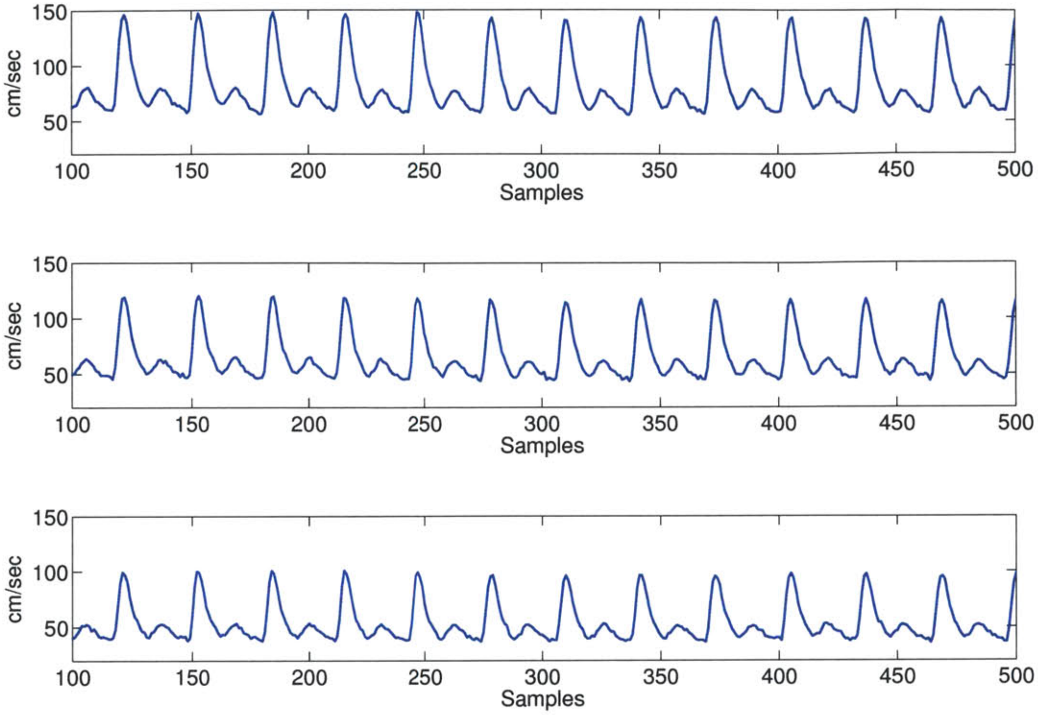

Figure 2.5: Simulated CBFV waveforms by varying R. From top to bottom, we used $R = 0.8, 1.0, 1.2 \ \frac{\text{ml}}{\text{sec}\cdot\text{mmHg}}$ with $C = 0.01 \ \frac{\text{ml}}{\text{mmHg}}$ and $L = 0.1 \ \frac{\text{mmHg}}{\text{ml/sec}}$. The sampling frequency is 50 Hz.

of the pulse width, and a faster transition. This corresponds to an accentuation of the high frequency components of the CBF waveform, which is characteristic of a capacitive element.

2.2.3 Kashif Model

Here, we describe an adaptation of the Ursino-Lodi model for ICP estimation. Using clinical measurements of ABP and CBF velocity (CBFV) waveforms as inputs, we seek to estimate the system parameters and ICP. However, for large-scale models, parameter estimation is often ill-posed meaning that the waveform data is not rich enough to reliably identify the model parameters. Even with seven parameters, the Ursino Lodi model is too complex to be reliably used for ICP estimation.

In [11], Kashif *et al.* observed that the generation and the reabsorption of CSF are much slower than the perfusion of blood through the brain. Over the short duration of a few beats, R_f and R_o in the Ursino-Lodi model can be approximated as open circuits. By combining the remaining resistors and capacitors, the Ursino-Lodi model can be reduced as shown in Figure 2.4A.

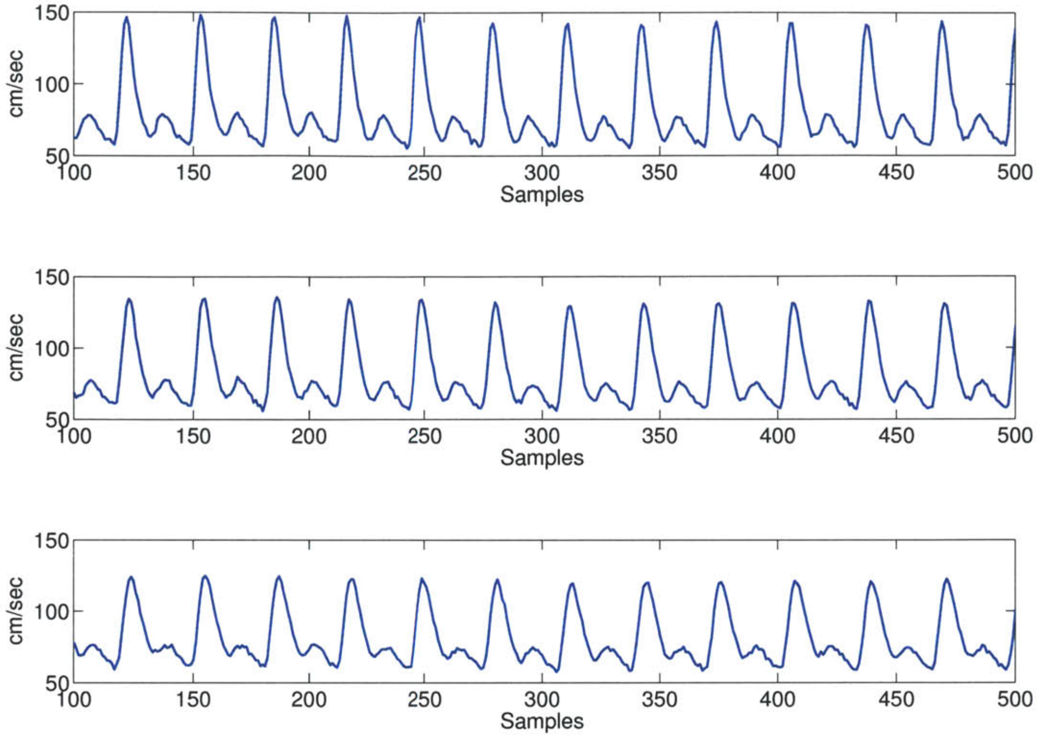

Figure 2.6: Simulated CBFV waveforms by varying L. From top to bottom, we used $L = 0.1, 0.3, 0.5\ \frac{\text{mmHg}}{\text{ml/sec}}$ with $R = 0.8\ \frac{\text{ml}}{\text{sec}\cdot\text{mmHg}}$ and $C = 0.01\ \frac{\text{ml}}{\text{mmHg}}$. The sampling frequency is 50 Hz.

We can represent the dynamics of this model by the following first-order differential equation

$$q(t) = \frac{p(t) - ICP}{R} + C\frac{dp(t)}{dt} \tag{2.9}$$

where $q(t)$ and $p(t)$ are the CBF and ABP waveforms, respectively; and R and C represent the variable, lumped resistive and capacitive properties of the cerebrovascular system and brain tissue. The Kashif model makes no assumption about the constancy of the cerebral space. It can therefore represent the entire brain or a major vascular territory, depending on the available pressure and flow measurement.

2.3 Model-based ICP Estimation

The model-based ICP estimation algorithm developed by Kashif takes as input windowed segments of ABP and CBFV (rather than CBF) waveforms over which the parameters, R and C, are assumed to be constant.

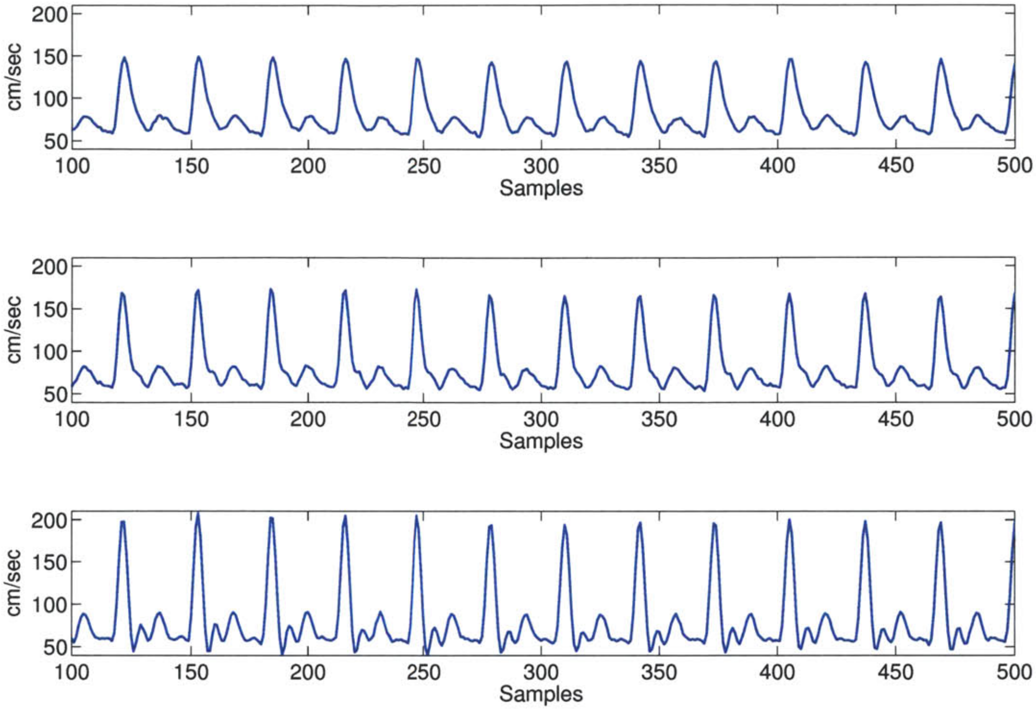

Figure 2.7: Simulated CBFV waveforms by varying C. From top to bottom, we used $C = 0.01, 0.03, 0.05$ $\frac{\text{ml}}{\text{mmHg}}$ with $R = 0.8$ $\frac{\text{ml}}{\text{sec}\cdot\text{mmHg}}$ and $L = 0.1$ $\frac{\text{mmHg}}{\text{ml/sec}}$. The sampling frequency is 50 Hz.

We show in Appendix B that with the use of CBFV, instead of CBF assuming a multiplicative relationship, ICP can still be recovered. The algorithm proceeds in stages by first estimating the capacitance and then the resistance using the waveform time series:

1. During the systolic upstroke, we can approximate (2.9) as

$$q(t) \quad \approx \quad C\frac{dp(t)}{dt} \tag{2.10}$$

Denoting t_0 and t_1 as the start and end of the systolic upstroke, respectively, we can rewrite (2.10) as

$$\int_{t=t_0}^{t_1} q(t)dt \quad \approx \quad C(p(t_1) - p(t_0)) \tag{2.11}$$

The lumped capacitance is taken to be the value of C that minimizes the mean squared error in fitting (2.11) at each ABP and CBFV wavelet in the estimation window.

2. With an estimate of C, we rewrite (2.9) as

$$q_1(t) = q(t) - C\frac{dp(t)}{dt} = \frac{p(t) - ICP}{R} \tag{2.12}$$

To minimize the noise that comes with differentiating the ABP waveform, for each ABP wavelet, we consider two points of low slope, denoted here as t_2 and t_3, respectively. Taking the difference of (2.12) evaluated at t_3 and t_2, we express R exclusively in terms of the input data

$$q_1(t_3) - q_1(t_2) = \frac{p(t_3) - p(t_2)}{R} \tag{2.13}$$

To estimate the lumped resistance, we choose R that minimizes the mean squared error in fitting (2.13) at each ABP and CBFV wavelet in the estimation window. With an estimate of R, ICP can be written in terms of the input data

$$ICP = MABP - R \cdot MCBFV \tag{2.14}$$

where $MABP$ and $MCBFV$ are the mean ABP and mean CBFV over the estimation window, respectively.

This approach is repeated for all non-overlapping windowed segments of ABP and CBFV.

This approach has been validated on 37 patients with traumatic brain injuries at Cambridge University's Addenbrooke Hospital with a mean bias of 1.5 mmHg and a standard deviation of error of 5.9 mmHg. This is comparable to certain noninvasive measurement modalities of ICP [11].

This algorithm is not without limitations. One major limitation is that the algorithm requires the input signals to be physiologically aligned. While the CBFV waveform is measured from the cerebral arteries, the ABP waveform is usually measured by radial artery catheterization. Consequently, we must apply a time-offset to shift the ABP waveform relative to the CBFV waveform to account for the difference in the propagation distance between the heart and the radial artery, where the ABP is measured, and the heart and the cerebral arteries, where the CBFV is measured. Using the same model, Kashif *et al.* propose algorithms that use the ABP and CBFV waveforms to determine this time-offset. Given the intrinsic difficulty of obtaining a stable CBFV waveform, estimating the time-offset is difficult, and different approaches to estimating the time-offset can generally yield different offset values. We describe Kashif's time-offset estimation algorithm in Appendix C.

Another limitation is the estimation of R, from which ICP is then estimated. In the Kashif algorithm, R is estimated by first finding the resistive current $q_1(t)$ which requires differentiating the ABP waveform. In practice, differentiating real data introduces high frequency noise that affects the parameter estimate of R. We argue that if this noise can be reduced, then we can increase the robustness of the parameter estimation. In the next chapter, we describe two algorithms that addresses the latter limitations.

Chapter 3

ICP Estimation

In the Kashif algorithm, a critical preprocessing step involves applying a time-offset to shift the measured arterial blood pressure (ABP) waveform relative to the cerebral blood flow velocity (CBFV) waveform to account for the difference in the propagation path between the heart and the middle cerebral artery, where the CBFV is measured, and the heart and the radial artery, where the ABP is measured. The estimation approach results are very sensitive to this time-offset, and estimating it can be difficult due to the distortion and artifacts present in the CBFV waveform. Here, we present two potential solutions to overcome this sensitivity.

First, we describe a simplified heuristic to estimate the time-offset. Then, we present a spectral-density (SD) based algorithm for intracranial pressure (ICP) estimation that does not require a temporal adjustment of our input data. We use this algorithm to first estimate the parameters of the inductive model of the cerebrovascular system and then ICP. We conclude with a summary of the techniques developed.

3.1 Time-Offset Determination Heuristic

The success of the Kashif algorithm depends on the time-offset chosen to shift the measured ABP waveform. Here, we describe a heuristic to estimate this time-offset. When the Kashif algorithm is applied to certain datasets, we first observe that many time-offset candidates result in negative ICP estimates for substantial stretches of the record length. Furthermore, for most patient records, we found that incrementing the time-offset (advancing the ABP waveform in time) increases the mean value of the ICP estimates. Finally, there exists a time-offset, τ^* that serves a transition point, such that all of the estimates obtained with time-offsets less than τ^* are negative for most of the record length. In contrast, estimates obtained by applying time-offsets greater than or equal to τ^* tend to be positive.

From these observations, we formulate the following algorithm to find τ^*. Using the ABP and CBFV waveforms, estimate ICP using the Kashif algorithm. At this stage, the time-offset parameter is initialized to 0.

- If the ICP estimates are negative for more than 10% of the record length, increment the time-offset parameter by one sampling interval and re-estimate ICP using the Kashif algorithm. In this scenario, we increment the time-offset parameter until the resulting ICP estimate is positive for more than 90% of the record length. This time-offset is τ^*.
- If the ICP estimate is positive for the entire record length, decrement the time-offset parameter and re-estimate ICP using the Kashif algorithm. Here, we continue decrementing the time-offset parameter until the resulting ICP estimate is positive for at least 90% of the record length. In this scenario, if we decremented the time offset again, the resulting ICP estimate would be negative for more than 10% of the record length. This time-offset is τ^*.

By construction, the heuristic biases the selection of the time-offset to produce ICP estimates with low mean values. Throughout this thesis, we will refer to this heuristic as the time-domain (TD) algorithm. In the next chapter, we examine the accuracy and precision of this approach and compare it to the time-offset algorithm used by Kashif.

3.2 Spectral Density Approach to Model Based ICP Estimation

In the last chapter, the inductive model of the cerebrovascular system was introduced. This representation relates the cerebral perfusion pressure (CPP), which is the pressure difference between ABP and ICP, to cerebral blood flow (CBF) in a three-parameter model, shown in Figure 3.1.

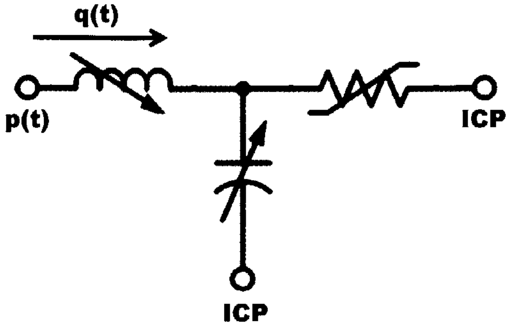

Figure 3.1: Inductive model of the cerebrovascular system.

We denote CPP and CBF as $x(t)$ and $q(t)$, respectively. This model is thus described by the following second-order differential equation:

$$q(t) + \frac{L}{R}\frac{dq(t)}{dt} + LC\frac{d^2q(t)}{dt^2} = \frac{x(t)}{R} + C\frac{dx(t)}{dt} \tag{3.1}$$

where R is the lumped cerebrovascular resistance, L is the aggregate inductance of the blood, and C is the aggregate arterial and brain tissue compliance. We will conduct the estimation of R, L, and C over a window of data over which we assume these parameters to remain constant.

Here, we take a spectral approach to estimating the model parameters. We define the spectral density of a signal to be the squared magnitude of its Fourier Transform. If we consider the spectral densities of $x(t)$ and $q(t)$, we obtain

$$|Q(j\omega)|^2\left(\left(1-\omega^2LC\right)^2 + \left(\frac{\omega L}{R}\right)^2\right) = |X(j\omega)|^2\left(\frac{1}{R^2} + (\omega C)^2\right) \tag{3.2}$$

where $|Q(j\omega)|^2$ and $|X(j\omega)|^2$ are the spectral densities of $q(t)$ and $x(t)$, respectively.

Ideally, we estimate the parameters, by first computing the spectra of CPP and CBFV over an estimation window, and then optimizing over the parameters to minimize the mean squared error in fitting the spectral densities of $x(t)$ and $q(t)$ to (3.2). However, since CPP cannot be measured noninvasively, we represent CPP over the duration of an estimation window by:

$$x(t) = p(t) - p_{ICP}(t) \approx p(t) - (\overline{p_{ICP}} + \alpha(p(t) - \overline{p})) \tag{3.3}$$

where $p(t)$ is the ABP waveform; $p_{ICP}(t)$ is the ICP waveform; $\overline{p}$ is the mean arterial pressure and $\overline{p_{ICP}}$ is the mean ICP over the estimation window; and $\alpha \in (0,1)$ is a scale factor applied to the ABP wavelet to approximate the ICP wavelet. This representation of CPP takes into account that ICP is a waveform with its own intrabeat pulsatility, and assumes the major pulsatile component of ICP, the percussion wave, is driven by the sharp onset of the ABP waveform.

Using this approximation, we can then rewrite (3.2). For $\omega > 0$, we have:

$$|Q(j\omega)|^2\left(\left(1-\omega^2LC\right)^2 + \left(\frac{\omega L}{R}\right)^2\right) = |(1-\alpha)P(j\omega)|^2\left(\frac{1}{R^2} + (C\omega)^2\right) \tag{3.4}$$

where $|P(j\omega)|^2$ is the spectral density of the ABP signal. After we estimate the parameters in (3.4), ICP can be written in terms of the averages of our input data:

$$\overline{p_{ICP}} = \overline{p} - R\overline{q} \tag{3.5}$$

where $\overline{q}$ is the mean blood flow. One caveat relates to the fact that instead of CBF, we have only CBF velocity (CBFV) available as a measurement. We substitute CBFV for CBF. Similar to the Kashif algorithm, it can be shown that ICP can still be recovered.

In the following sections, we discuss the selection of frequencies and α used in identifying the system parameters.

3.2.1 Frequency Selection

ABP and CBFV are quasi-periodic waveforms. For $\omega > 0$, most of the signal energy is concentrated in the first few harmonic frequencies. In Figure 3.1, we plot an example of the spectral density of a windowed segment of the ABP waveform.

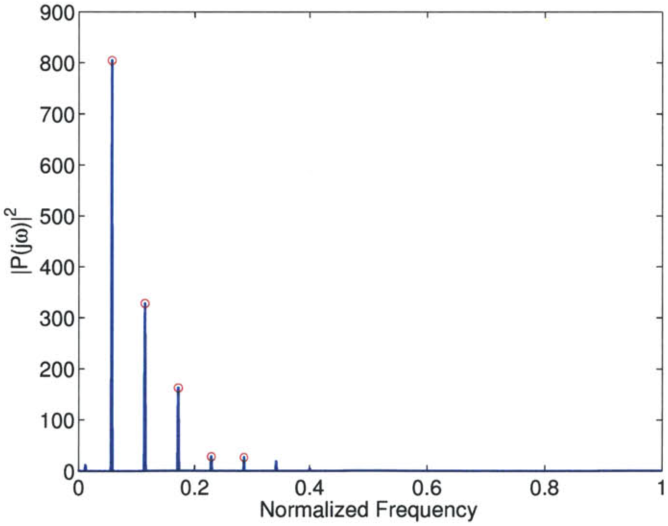

Figure 3.2: Spectral density of ABP waveform.

As these signals are driven by the cardiac frequency, the fundamental frequency of both waveforms corresponds to the patient's heart rate. Motivated by this observation, we estimate the system parameters by minimizing the residual error in fitting the spectral densities of ABP and CBFV to (3.4) at the harmonic frequencies. To estimate the fundamental frequency, we first extract the heart rate from the ABP signal by applying a beat-onset detection algorithm [23] to our ABP data, and calculate the heart rate using the mean interbeat interval.

3.2.2 Selection of α

To reflect the fact that the percussion wave of the ICP waveform is driven by the pulsatility of ABP, we approximate the intrabeat pulsatility of the ICP waveform by scaling the mean-subtracted ABP signal. In both wavelets, the fundamental frequency is most prominent in terms of signal energy. Therefore, to approximate the pulsatility of ICP, we choose α such that the approximation in (3.3) has the same spectral density as the actual ICP waveform at the fundamental frequency. In the time-domain, this approximately corresponds to scaling the peak-to-peak magnitude of the ABP wavelet to be equal to that of the ICP wavelet.

As the peak-to-peak magnitude of the ICP wavelet is not known, we approximate it as 5 mmHg. The peak-to-peak magnitude of the ABP waveform is the difference between the mean systolic and diastolic pressures over the stretch of ABP data. Using these facts, we see that α is equal to $\frac{5}{PP}$, where PP is the average peak-to-peak magnitude of the ABP waveform.

3.2.3 Parameter Estimation

With the selection of the harmonic frequencies and α, we now discuss the estimation of the parameters in (3.4). Rearranging the terms in (3.4), we have the equivalent relationship

$$|Q(j\omega)|^2 = (1-\alpha)^2|P(j\omega)|^2\left(\frac{1}{R^2}+C^2\omega^2\right)+\omega^2|Q(j\omega)|^2\left(2LC-\frac{L^2}{R^2}\right)-\omega^4L^2C^2|Q(j\omega)|^2 \tag{3.6}$$

Again, assuming that the parameters are constant over the duration of the estimation window, we can consider (3.6) at each harmonic frequency and condense the system of equations in matrix form. The estimation problem is then posed as the following quadratic program

$$\min_{v}\left\|\begin{bmatrix}|Q(j\omega_0)|^2\\ \vdots \\ |Q(jk\omega_0)|^2\end{bmatrix}-\begin{bmatrix}(1-\alpha)^2|P(j\omega_0)|^2 & (1-\alpha)^2\omega_0^2|P(j\omega_0)|^2 & -\omega_0^2|Q(j\omega_0)|^2 & -\omega_0^4|Q(j\omega_0)|^2\\ \vdots & \vdots & \vdots & \vdots \\ (1-\alpha)^2|P(jk\omega_0)|^2 & (1-\alpha)^2k^2\omega_0^2|P(jk\omega_0)|^2 & -k^2\omega_0^2|Q(jk\omega_0)|^2 & -k^4\omega_0^4|Q(jk\omega_0)|^2\end{bmatrix}\vec{v}\right\|_2^2 \tag{3.7}$$

$$\begin{aligned} \text{subject to} \quad & \frac{v_1 v_4}{v_2} - 2\sqrt{v_4} = v_3 && (3.8) \\ & v_1 > 0 && (3.9) \\ & v_2 > 0 && (3.10) \\ & v_4 > 0 && (3.11) \end{aligned}$$

where k is the number of harmonics used to estimate our parameters and $v = (v_1, v_2, v_3, v_4)^T$ such that $v_1 = \frac{1}{R^2}$, $v_2 = C^2$, $v_3 = \frac{L^2}{R^2} - 2LC$, and $v_4 = L^2C^2$. To estimate the parameters and then ICP, we have $k = 5$. We relax our constraints further by eliminating (3.8). We then find the optimal parameters in the following formulation

$$\min_{v} \left\| \begin{bmatrix} |Q(j\omega_0)|^2 \\ \vdots \\ Q(jk\omega_0)|^2 \end{bmatrix} - \begin{bmatrix} (1-\alpha)^2|P(j\omega_0)|^2 & (1-\alpha)^2\omega_0^2|P(j\omega_0)|^2 & -\omega_0^2|Q(j\omega_0)|^2 & -\omega_0^4|Q(j\omega_0)|^2 \\ \vdots & \vdots & \vdots & \vdots \\ (1-\alpha)^2|P(jk\omega_0)|^2 & (1-\alpha)^2k^2\omega_0^2|P(jk\omega_0)|^2 & -k^2\omega_0^2|Q(jk\omega_0)|^2 & -k^4\omega_0^4|Q(jk\omega_0)|^2 \end{bmatrix} \vec{v} \right\|_2^2 \quad (3.12)$$

$$\begin{aligned} \text{subject to} \quad & v_1 > 0 && (3.13) \\ & v_2 > 0 && (3.14) \\ & v_4 > 0 && (3.15) \end{aligned}$$

For each data record, we repeat this procedure for consecutive, non-overlapping windows to produce estimates of ICP for the entire duration of the record.

3.2.3.1 Estimation in the Presence of Noise

In our datasets, the ABP waveform signal is relatively noise-free. In contrast, the CBFV waveform can be very noisy. Given the importance of the ABP and CBFV waveforms in estimating the system parameters, we describe techniques to mitigate the effect of such noise.

Due to the potentially poor signal quality of the CBFV waveform, the spectral density of CBFV can have a degree of variability across consecutive windows, resulting in ICP estimates with unphysiological fluctuations. We considered three different approaches to reduce this window-to-window variability by further subdividing each estimation window into N smaller, non-overlapping segments. N is chosen to ensure that the length of each sub-window is an integer multiple of the interbeat interval to minimize the effect of spectral leakage. (Spectral leakage corresponds to the blurring of the spectral density and arises from the truncation of the continuous waveform into non-overlapping estimation windows.)

Below, we list the three approaches (M1-M3) we used to reduce variability in our estimation of the CBFV spectral density.

M1 For each sub-window, we estimate the parameters by solving (3.12). To generate our parameter estimates for the overall window, we average the N sub-window parameter estimates, on a window-by-window basis.

M2 We average the N density functions computed from each sub-window. With the averaged density function, we estimate the parameters by solving (3.12).

M3 For each sub-window, we consider the matrix A_i and vector b_i such that $||b_i - A_i v||_2^2$ corresponds to the objective function in (3.12) as if we were estimating the parameters for each sub-window. Instead, here, we solve:

$$\min_v \left\| \begin{bmatrix} b_1 \\ \vdots \\ b_n \end{bmatrix} - \begin{bmatrix} A_1 \\ \vdots \\ A_n \end{bmatrix} \vec{v} \right\|_2^2 \quad s.t. \quad v_1, v_2, v_4 > 0$$

3.3 Summary

We summarize two algorithms developed to address the limitations of the Kashif algorithm.

Time-Domain (TD) Algorithm We present a heuristic to determine time-offset parameter for the Kashif algorithm. The output of this algorithm results in the optimal time-offset and the ICP estimate time series.

Using the ABP and CBFV waveforms, with the time-offset parameter initialized to 0, estimate ICP using the Kashif algorithm.

- If the ICP estimates are negative for more than 10% of the record length, increment the time-offset parameter and re-estimate ICP using the Kashif algorithm. In this scenario, we increment the time-offset parameter until the resulting ICP estimate is positive for more than 90% of the record length. This time-offset is τ^*.
- If the ICP estimate is positive for the entire record length, decrement the time-offset parameter and re-estimate ICP using the Kashif algorithm. Here, we continue decrementing the time-offset parameter

until the resulting ICP estimate is positive for at least 90% of the record length. In this scenario, if we decremented the time offset again, the resulting ICP estimate would be negative for more than 10% of the record length. This time-offset is τ^*.

Spectral-Density(SD) Algorithm We present an overview of the preprocessing and estimation steps involved in identifying the system parameters and then ICP in the inductive model of the cerebrovascular system.

1. Divide the time-locked ABP and CBFV waveforms into non-overlapping windows. Each window is comprised of 60 cardiac cycles.
2. For each window, compute α by first computing the difference between the mean systolic and diastolic pressures. α is then equal to $\frac{5}{PP}$, where PP corresponds to the difference between the mean systolic and diastolic pressures.
3. Estimate the parameters, R, L, and C, using method M1 and (3.12).
4. The ICP estimate for the window is found by evaluating the expression in (3.5).

In the next chapter, we present the results of our ICP estimates and compare it against the invasively measured signal.

Chapter 4

Results and Discussions

We present the performance of the spectral-density (SD) and time-domain (TD) approaches introduced in the preceding chapter for estimating intracranial pressure (ICP) in both simulated and clinical datasets. We first describe the results of applying the algorithms to arterial blood pressure (ABP) and simulated cerebral blood flow velocity (CBFV) waveforms using two models of cerebrovascular physiology. We compare the performances of the SD and TD algorithms in estimating ICP from the simulated data, and summarize the results and insight gained from this study. In the latter half of this chapter, we apply the algorithms to ABP and CBFV waveforms collected from patients with traumatic brain injuries. Similar to the simulation study, we summarize and compare the performance of both algorithms and discuss potential sources of estimation error. We conclude with a summary of this chapter.

4.1 Simulated Dataset

In this section, we describe the performance of the SD and TD algorithms on simulated patient data. For each record, we use clinical ABP and ICP waveforms measured from eight patients with traumatic brain injuries to simulate CBFV waveforms using the approach outlined in Section 2.2. In total, we simulated 64 patient records, choosing $R \in [0.8, 1.2]\ \frac{\text{mL}}{\text{s}\cdot\text{mmHg}}$, $L \in [0.01, 0.1]\ \frac{\text{mmHg}}{\text{ml/sec}}$, and $C \in [0.01, 0.05]\ \frac{\text{ml}}{\text{mmHg}}$. The benefit of conducting this simulation study is the fact that we can control the parameter values and impose a known ICP waveform in simulating the CBFV waveform to identify the limitations of both approaches.

In the first half of this section, we simulate CBFV waveforms using the Kashif model of the cerebrovascular system. We seek to quantify the performances of the SD and TD algorithms under the ideal conditions assumed by Kashif, namely that the cerebrovascular system is described by his model. We simulate CBFV by imposing both constant and pulsatile ICP and analyze the robustness of both estimation approaches. In the latter half of this section, we simulate CBFV using the inductive model of the cerebrovascular system by imposing both constant and pulsatile ICP. The inductive model was chosen as it is structurally different from the model from which the TD algorithm is derived. It is therefore expected that the estimation task is harder than with the Kashif model. Furthermore, the TD approach relies on a detailed analysis of the waveform morphology, which is affected by the inertial properties of blood. The inductive model is the model underlying our SD algorithm, so we expect the SD algorithm to perform well in its estimation task on data simulated with the inductive model. We describe the performance of the SD and TD algorithms and quantify the effect of the structured modeling error on the TD algorithm.

4.1.1 Kashif Model

We present the results of applying the SD and TD algorithm to 64 patient records simulated using the Kashif model of the cerebrovascular system. Of the 64 records, equal proportions were obtained by simulating CBFV with constant and pulsatile ICP, respectively. In total, we obtain 224 non-overlapping windows of data, each of which is 60 cardiac cycles long, from which ICP is then estimated. First, we present the results for the records simulated with constant ICP.

4.1.1.1 CBFV simulated with constant ICP

For the SD algorithm, the mean error (bias) is -0.1 mmHg, the standard deviation of error (SDE) is 0.7 mmHg, and the root-mean-squared error (RMSE) is 0.7 mmHg. The bias relates to the accuracy of the algorithm, whereas the SDE relates to its precision. The RMSE combines both the accuracy and precision into a single metric, and is equal to the geometric mean of the SDE and bias. Given that the ICP used in this simulation is constant, we set α to 0 in the SD algorithm.

We summarize the error statistics in a Bland-Altman plot, in Figure 4.1. The clusters in Figure 4.1 are artifacts of the fact that 8 patients were used to generate the 32 records with different parameter choices. The clusters arise due to the low bias of the ICP estimates.

For the TD algorithm, the bias is 5.5 mmHg, the SDE is 8.4 mmHg, and the RMSE is 10.0 mmHg. We summarize these results in Figure 4.2. The diagonal striations in Figure 4.2 are artifacts of the fact that eight patients were used to generate the 32 records. Each clinical record was used to generate four distinct CBFV waveforms. With each parameter setting, the bias of the ICP estimates changes in this approach. Furthermore, the positive bias and comparatively large SDE are expected because the non-negativity metric of the TD algorithm biases the ICP estimates to be low. In these eight patient records, a large majority of the ICP waveforms have mean values that exceed 20 mmHg.

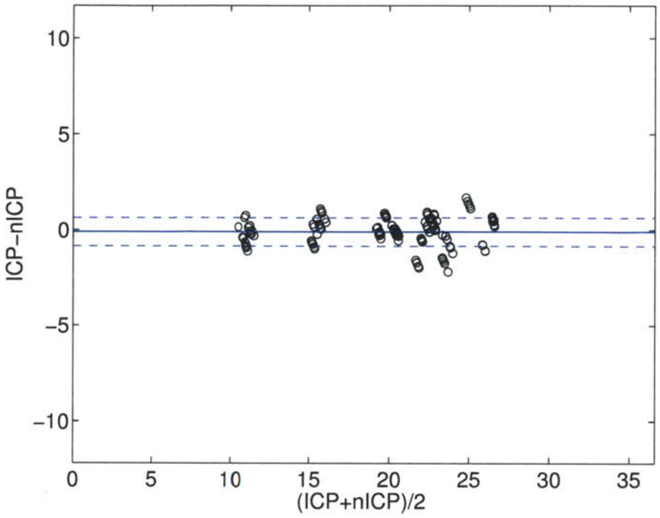

Figure 4.1: Bland-Altman plot of simulated data (with constant ICP) using SD algorithm. The bias is −0.1 mmHg and the SDE is 0.7 mmHg.

Comparing the two algorithms, we see that under the ideal conditions of the Kashif algorithm, the SD algorithm is more precise and accurate than the TD algorithm with essentially zero bias and minimal SDE. Next, we examine the robustness of both approaches when the CBFV waveform is simulated with pulsatile ICP.

4.1.1.2 CBFV simulated with pulsatile ICP

For the SD algorithm, the bias is 0.0 mmHg, the SDE is 2.0 mmHg, and the RMSE is 2.0 mmHg. Given that the ICP used in this simulation is pulsatile, we set α to $\frac{5}{\mathrm{PP}}$, where PP is the average pulse-pressure computed over each estimation window. We summarize the error statistics in Figure 4.3.

Compared to the ICP estimates for the records for which the CBFV waveforms were simulated using constant ICP, the ICP estimates here have a larger SDE. This is due to the approximation of the ICP pulsatility through the scaled pulsatility of ABP, which assumes that the peak-peak magnitude of the ICP waveform is consistently 5 mmHg. We know from [5] that as the mean ICP increases, the peak-peak magnitude of the waveform also increases. As this is not reflected in the algorithm, the performance deteriorates.

For the TD algorithm, the bias is 5.2 mmHg, the SDE is 6.7 mmHg, and the RMSE is 8.5 mmHg. We summarize these results in Figure 4.4. Here, we observe that the error statistics are relatively unchanged when compared to those of the records where the CBFV waveform was generated with constant ICP.

Again, we see that the SD algorithm is more accurate and precise than the TD algorithm. Next, we examine the performance of both algorithms when CBFV is generated using the inductive model of the

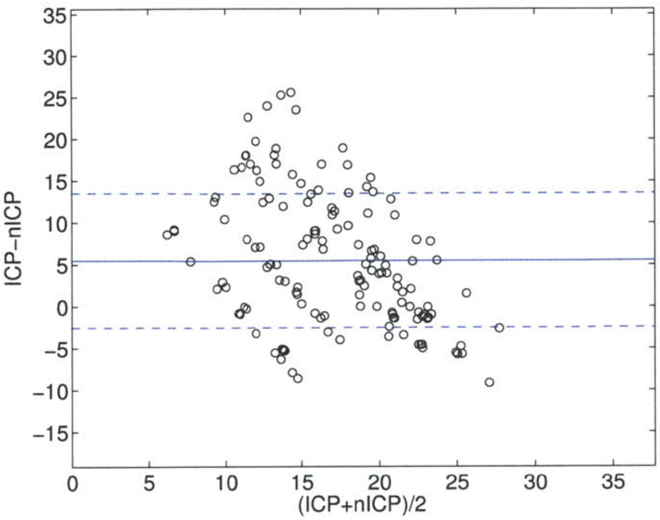

Figure 4.2: Bland-Altman plot of simulated data (with constant ICP) using TD algorithm. The bias is 5.5 mmHg and the SDE is 8.4 mmHg.

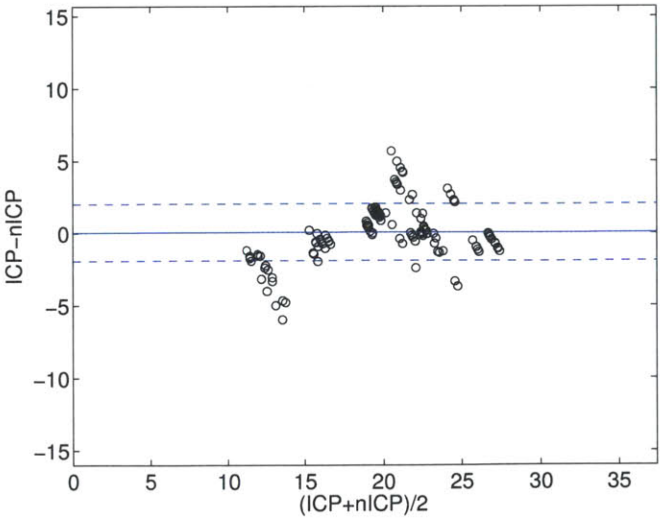

Figure 4.3: Bland-Altman plot of simulated data (with pulsatile ICP) using SD algorithm. The bias is 0.0 mmHg and the SDE is 2.0 mmHg.

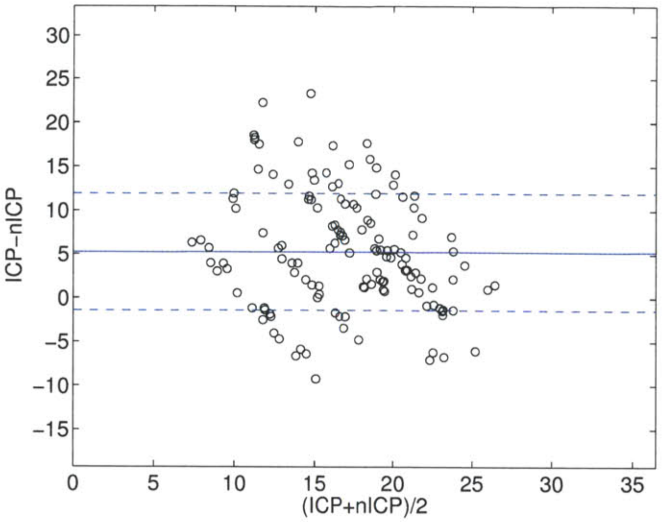

Figure 4.4: Bland-Altman plot of simulated data (with pulsatile ICP) using TD algorithm. The bias is 5.2 mmHg and the SDE is 6.7 mmHg.

cerebrovascular system.

4.1.2 Inductive Model

We present the results of applying the SD and TD algorithm to 64 patient records simulated using the inductive model of the cerebrovascular system. Of the 64 records, equal proportions were obtained by simulating CBFV with constant and pulsatile ICP, respectively. In total, we obtain 224 non-overlapping windows of data, each of which is 60 cardiac cycles long, from which ICP is then estimated. First, we present the results for the records simulated with constant ICP.

4.1.2.1 CBFV simulated with constant ICP

For the SD algorithm, the bias is −0.1 mmHg, the SDE is 0.9 mmHg, and the RMSE is 0.9 mmHg. We summarize these results in Figure 4.5. As the CBFV was generated using constant ICP, we set α to 0.

For the TD algorithm, the bias is 3.9 mmHg, the SDE is 9.4 mmHg, and the RMSE is 10.2 mmHg. We summarize these results in Figure 4.6. Compared to the records where CBFV was simulated using the Kashif model, we observe that the error statistics are comparable. This result suggests that the TD algorithm is robust against some degree of structured modeling error. We also observe that the SD algorithm is very accurate and very price when data are simulated with the inductive model. This is reassuring since the inductive model underlies the development of the SD estimation algorithm. In the next section, we repeat the same exercise using records where the CBFV waveform is simulated with pulsatile ICP.

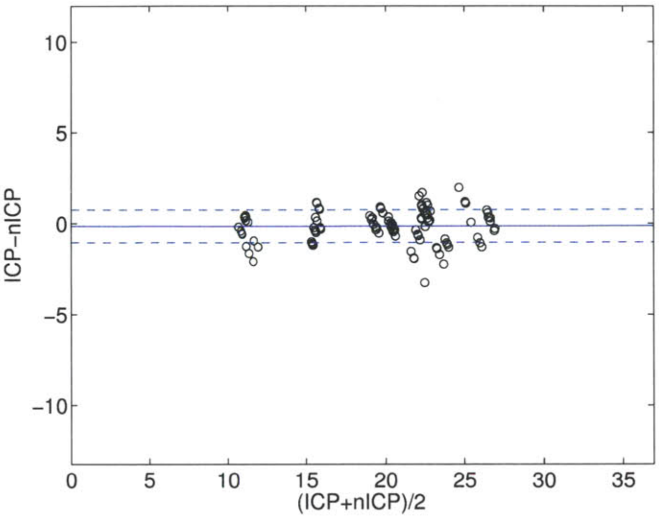

Figure 4.5: Bland-Altman plot of simulated data (with constant ICP) using SD algorithm. The bias is −0.1 mmHg and the SDE is 0.9 mmHg.

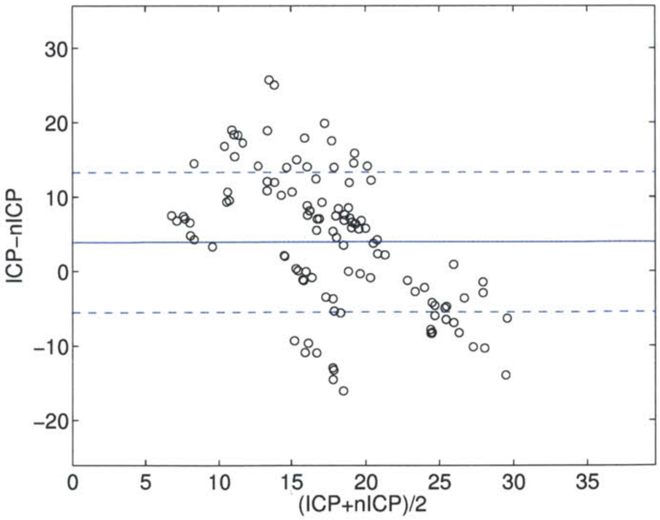

Figure 4.6: Bland-Altman plot of simulated data (with constant ICP) using TD algorithm. The bias is 3.9 mmHg and the SDE is 9.4 mmHg.

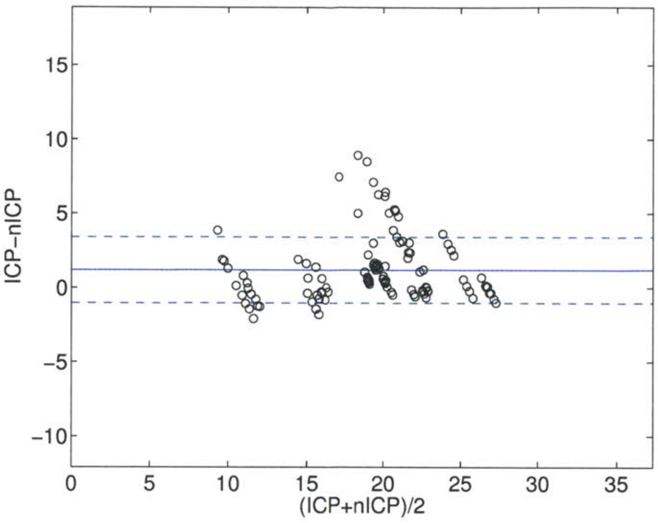

Figure 4.7: Bland-Altman plot of simulated data (using pulsatile ICP) using SD algorithm. The bias is 1.2 mmHg and the SDE is 2.2 mmHg.

4.1.2.2 CBFV simulated with pulsatile ICP

For the SD approach, across all non-overlapping estimates, the bias is 1.2 mmHg, the SDE is 2.2 mmHg, and the RMSE is 2.5 mmHg.

In Figure 4.7, we observe that certain ICP estimates have large mean errors. As we have stated earlier, this error is due to the underestimation of α. We found that when the approximation of the cerebral perfusion pressure (CPP) used in the SD algorithm is poor, the ICP estimates have large mean errors. In the SD algorithm, we approximate the pulsatility of the ICP waveform by scaling the pulsatility of the ABP waveform. For records with large bias (>5 mmHg), the average RMSE between the actual mean-subtracted CPP and its approximation is 15.6 mmHg. For records with low bias (<5 mmHg), the average RMSE between the actual mean-subtracted CPP and its approximation is 8.3 mmHg.

For the TD approach, across all non-overlapping estimates, the bias is 3.7 mmHg, the SDE is 9.8 mmHg, and the RMSE is 10.5 mmHg. Moreover, compared to the previous records where CBFV was simulated with constant ICP, the error statistics remain relatively unchanged. This suggests that the TD algorithm is again robust against structured modeling error. We summarize these results in Figure 4.8.

In our simulation study, we find that the SD algorithm is more accurate and precise than the TD algorithm, and that the error statistics of the TD algorithm remains essentially constant across the various simulation scenarios. This would suggest that the TD approach produces a robust lower bound on the true ICP, at least in the simulation study. Next, we apply both techniques to a clinical dataset of patients with traumatic brain injuries.

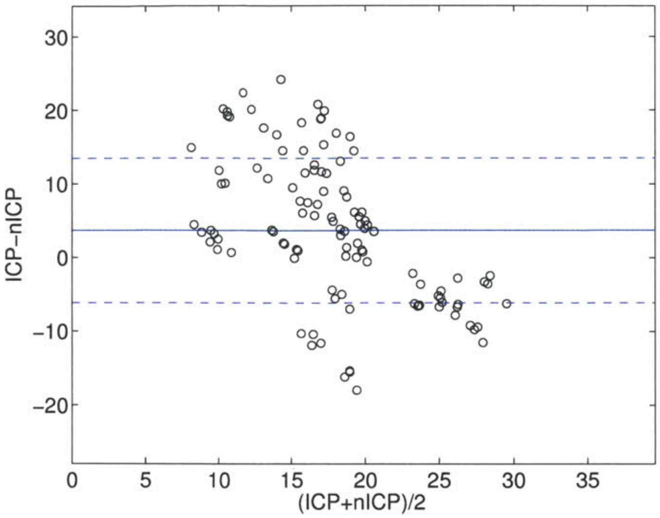

Figure 4.8: Bland-Altman plot of simulated data (using pulsatile ICP) using TD algorithm. The bias is 3.7 mmHg and the SDE is 9.8 mmHg.

4.2 Clinical Dataset

We describe the performance of SD and TD algorithm on 36 records collected from traumatic brain injury patients at Addenbrooke's Hospital in Cambridge University. This archived data was collected as part of routine clinical care in the neurocritical intensive care unit. Each record contains ABP waveforms measured from the radial artery, CBFV waveforms measured from both the right and left middle cerebral artery, and ICP waveforms measured with an intraparenchymal probe. The record length ranged from 6 minutes to 4 hours, with sampling frequencies ranging from 20 to 70 Hz.

We applied both algorithms to the ABP and CBFV waveforms for each patient record. When both left-sided and right-sided CBFV waveforms were available, we averaged the ICP estimates obtained from applying the algorithm separately to each unilateral CBFV waveform. For ICP estimates obtained using the SD algorithm, we ignored patient records in which the resulting ICP estimates were negative for more than 10% of the record length. In total, we discarded four patient records and analyzed the remaining 32 patient records.

In this dataset, the vertical displacement, denoted here as h, between the heart, the level at which the ABP measurements are calibrated, and the middle cerebral artery (MCA) is not known. The estimation algorithms assume that we have access to ABP at the level of the MCA. However. as a result of the hydrostatic pressure difference between the two locations, the mean pressure of the radial ABP overestimates the mean pressure of the ABP in the MCA if the patient is in the head-up position. Elevation of the head is a common supportive measure for brain injury patients to relieve intracranial congestion and the head of the bed is

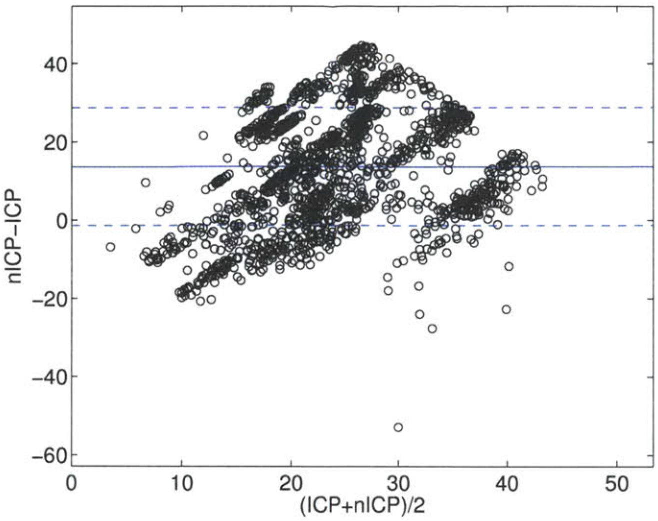

Figure 4.9: Bland-Altman plot of traumatic brain injury patients using SD algorithm. The bias is 13.7 mmHg and the SDE is 15.0 mmHg.

often tilted up by 20-30 degrees [7]. In [13], patients, for example, in the neurocritical intensive care unit have vertical displacements between the heart and the MCA of 15 cm to 30 cm, resulting in a pressure difference of 11 to 22 mmHg. We discuss the ramifications of not knowing the head position when we compare the ICP estimation approaches.

In the first half of this section, we describe the performance of the SD algorithm on this dataset. Here, we aggregate the estimation results, presenting them in a Bland Altman plot, and provide examples of ICP estimates. Moreover, we discuss sources of potential estimation error in the SD algorithm. In the latter half, we describe the performance of the TD algorithm on this dataset. As the TD algorithm was inspired by the Kashif algorithm, we compare its results directly to Kashif *et al.* and discuss discrepancies between the two algorithms. We conclude this section with a comparison of both algorithms.

4.2.1 SD Algorithm

We present the results of applying the SD algorithm to 32 patient records. From the 32 patient records, we obtained 1603 non-overlapping windows of data, for which ICP was estimated. The length of each non-overlapping window was 60 cardiac cycles. We compared each ICP estimate against the measured mean ICP across the same estimation window. Across all non-overlapping estimates, the bias is 13.7 mmHg, the SDE is 15.0 mmHg, and the RMSE is 20.3 mmHg. We summarize our results in Figure 4.9.

Figures 4.10 and 4.11 are examples of acceptable ICP estimates (denoted as *nICP)* plotted along with the invasively measured ICP (denoted as *ICP*). In both figures, the bias is within ±10 mmHg, which is comparable to certain intraparenchymal probes used to measure ICP, although clinically, such a discrepancy will surely be of concern. Furthermore, the trends in the measured ICP are also reflected in the estimates. For example, in Figure 4.10, we observe the ICP estimate increases at $t \approx 1100$ seconds and decreases at $t \approx 1500$ seconds corresponding to the clinical ICP. In all acceptable ICP estimates, we observe moderate high-frequency noise in the estimates. Later in this section, we discuss the potential sources of this noise.

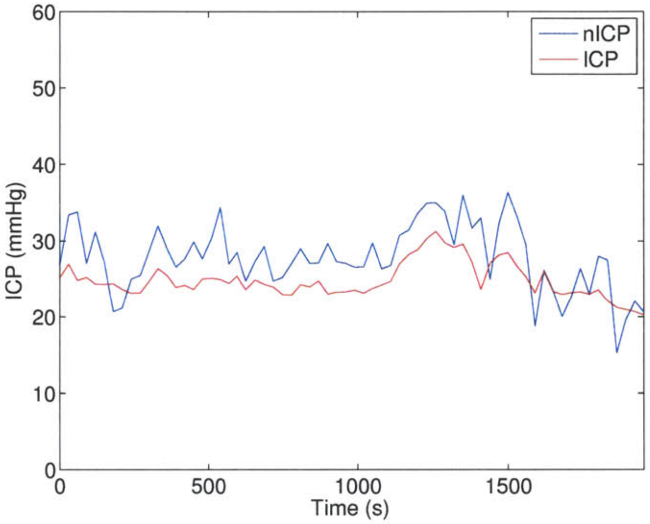

Figure 4.10: Example of good ICP estimate.

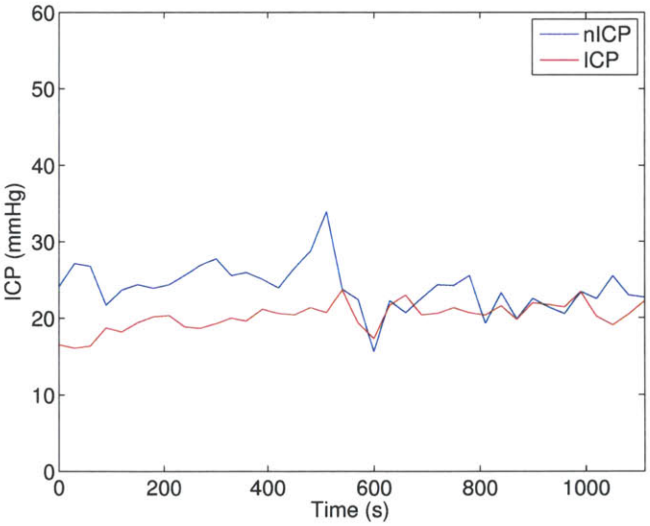

Figure 4.11: Example of good ICP estimate.

Figures 4.12 and 4.13 are examples of ICP estimates with systematic problems. In both of these estimates, the bias exceeds 20 mmHg. While such large mean errors are clearly unacceptable clinically, the trends in the ICP estimates reflect trends in the measured ICP. For example, in Figure 4.12, we see that the slight decrease in the measured ICP at $t \approx 200$ seconds is mirrored in the estimate as well.

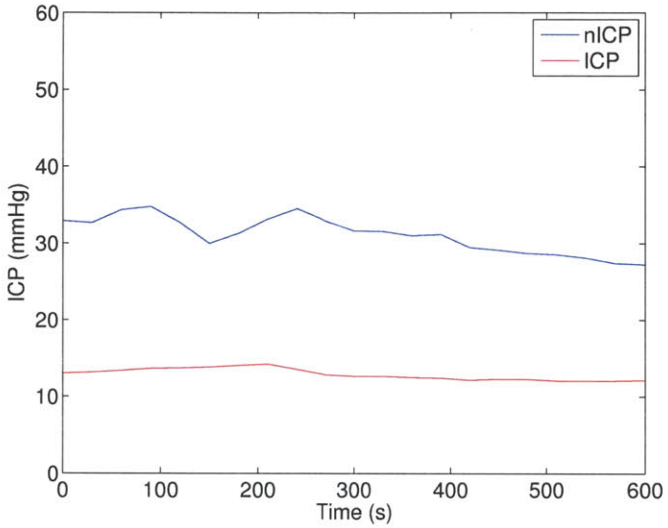

Figure 4.12: Example of ICP estimate with high bias.

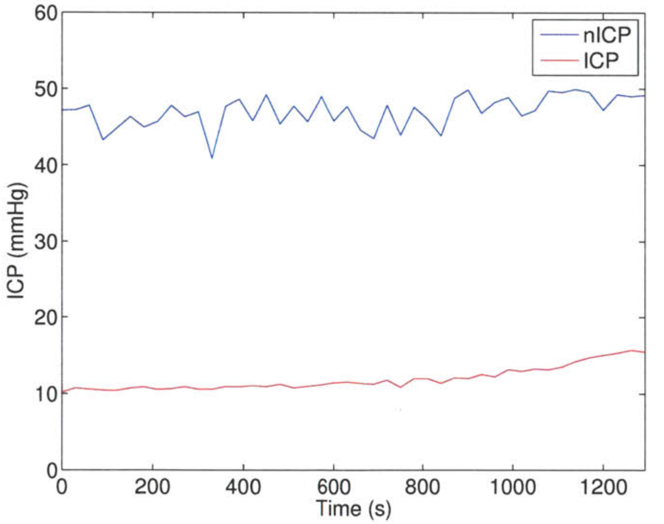

Figure 4.13: Example of ICP estimate with high bias.

Figures 4.14 and 4.15 are examples of unacceptable ICP estimates. In these examples, there is high bias and high variability across the entire record. For example, in Figure 4.15, the sharp increase in ICP at $t \approx 1000$ seconds is inverted in the estimated time series. In all of the unacceptable estimates, there is substantial high frequency noise in the estimated time series. In the next section, we describe potential sources of this noise in the estimation of ICP.

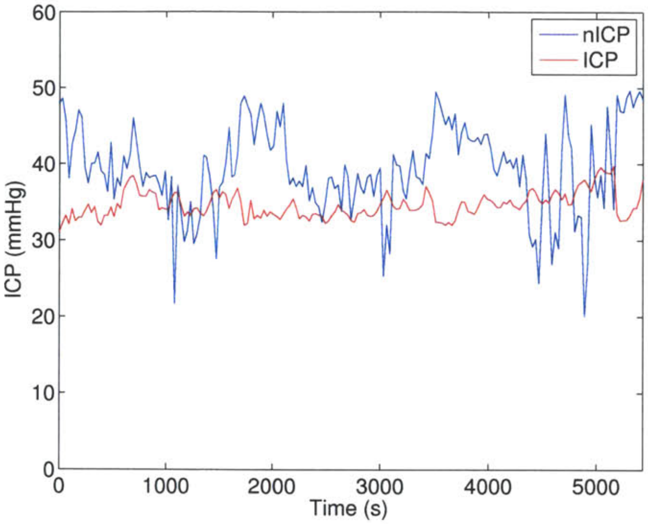

Figure 4.14: Example of ICP estimate with high bias and unphysiological variability.

4.2.1.1 Sources of estimation error

In the examples above, the ICP estimate have unacceptably high bias and SDE. Here, we list three potential reasons for this.

Lack of known h In this clinical dataset, the relative height between the ABP measurement location and MCA is not known. Since the patient population is drawn from patients with severe traumatic brain injuries, it is to be expected that all patients are in the head-up position. Consequently, we expect that our ICP estimates consistently overestimate the measured ICP, as the mean ABP is not adjusted. This is indeed the case. By knowing h, we believe that the overall bias of the ICP estimates will be lowered. This limitation is currently being addressed by our data collection at Boston's Beth Israel Deaconess Medical Center, where we measure the vertical distance between the ABP transducer location and the MCA.

Insufficiently rich data The SD algorithm requires the input data to be sufficiently rich, meaning that the spectrum of the input signals has to have enough harmonics to reliably estimate the system parameters and ICP. In our implementation of the SD algorithm, we require five harmonics. In many patient records, we find that there are not enough harmonics in the input data to reliably estimate the model parameters. For many estimation windows within this dataset, the spectrum of the CBFV waveform typically has only three visible harmonics (Figure 4.16). Without sufficiently rich data, ICP cannot be reliably estimated using the SD approach.

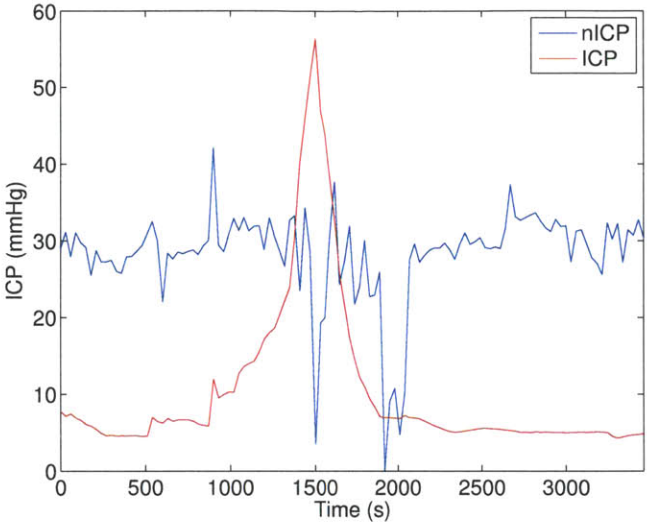

Figure 4.15: Example of ICP estimate with high bias and unphysiological variability.

Inaccurate signal representation In the SD algorithm, we approximate the pulsatility of the cerebral perfusion pressure (CPP) by scaling the pulsatility of the ABP waveform. This reflects the fact that the sharp intra-beat upstroke of the ICP waveform is driven by the onset of ABP. However, this approximation of CPP does not factor in the morphological differences between the ABP waveform measured in the radial artery and that measured at the MCA, resulting in a potentially poor approximation of CPP [14]. It should be kept in mind that throughout the simulation studies, we assumed access to both pressure and flow measured at the MCA. Approximating the MCA ABP waveform through radial artery pressure might introduce significant error in our estimation. As shown in the simulation study, a poor approximation of CPP often leads to significant bias in the ICP estimate.

4.2.2 TD Algorithm

We present the results of applying the TD algorithm to 32 patient records. From the 32 patient records, we obtained 1603 non-overlapping windows of data, for which ICP was estimated. Each non-overlapping window was comprised of 60 beats. We compared each ICP estimate against the measured mean ICP across the estimation window. Across all non-overlapping estimates, the mean bias is 2.9 mmHg, the SDE is 9.9 mmHg, and the RMSE is 10.32. We summarize our results in Figure 4.17. Comparing the error statistics of the TD and SD algorithms, we see that the TD algorithm outperforms the SD algorithm in both bias and SDE. We discuss reasons for this in the next section.

Using the same dataset, Kashif *et al.* report a bias of 1.5 mmHg and SDE of 5.9 mmHg. The difference between the TD algorithm and the approach in [11] is the selection of the time-offset applied to the ABP

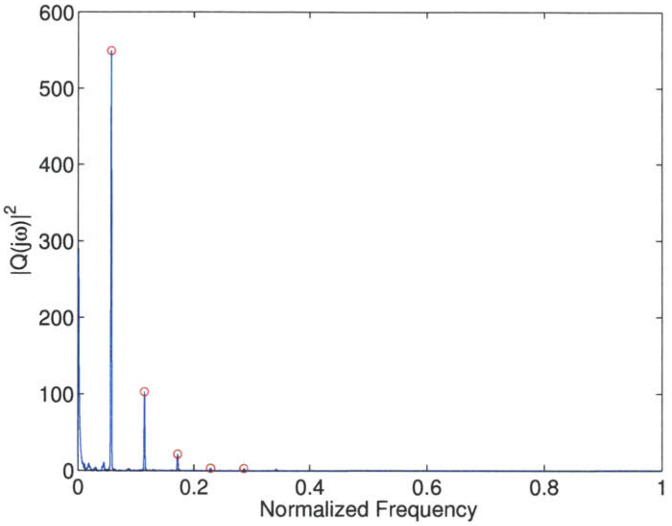

Figure 4.16: The spectral density of CBFV. Harmonic magnitudes are indicated by the red circles.

and CBFV waveforms. In [11], the time-offset was computed using an algorithm described in Appendix B, whereas in the TD algorithm, we use the non-negativity heuristic, described in Chapter 3, to determine the offset. Here, we see that the error statistics of the TD algorithm is comparable to the error statistics presented in [11]. The higher bias and SDE is due to the fact that the TD algorithm favors ICP estimates to be low whereas high ICP are encountered in patients with traumatic brain injuries. This comparison suggests that for injuries in which the ICP are moderate (i.e. strokes, hydrocephalus, etc.) the TD algorithm provides a good approximation of the approach in [11].

4.2.3 Comparison of SD and TD Approach

Unlike the simulated dataset, we observe that the TD algorithm outperformed the SD algorithm when both are applied to the clinical dataset. Here, we consider the potential effect of the hydrostatic pressure on our estimation results. The TD approach is less affected by the hydrostatic pressure since the time-offset is chosen to ensure that the ICP estimate is positive for more than 90% of the record duration. Here, we analyze the effect of the hydrostatic pressure on the SD algorithm.

The ICP estimates derived by the SD approach have two types of errors: one due to the hydrostatic pressure difference and another due to estimation. This motivates the question of whether knowledge of h would reduce both the bias and the SDE. Without the direct measurement of the vertical displacement, we assume that h is uniformly sampled from $[15, 30]$ cm. The bias is computed as follows:

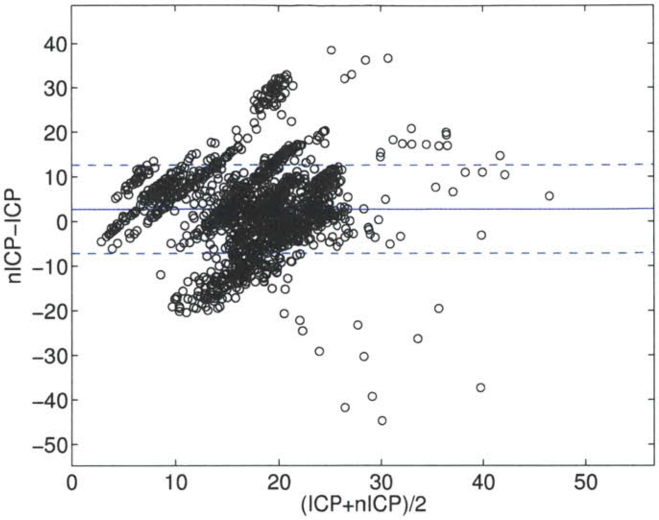

Figure 4.17: Bland-Altman plot of traumatic brain injury patients using TD algorithm.

$$\mu \;=\; \frac{1}{n}\sum_{i=1}^{n}(\widehat{ICP}_i + \rho g h_i - ICP_i) \tag{4.1}$$

where $\widehat{ICP}_i$ and ICP_i is the ICP estimate and mean ICP for the i^{th} window; ρ is the density of blood; g is the gravitational constant; and h_i is the vertical displacement between the level of the heart and the level of the middle cerebral artery corresponding to the i^{th} window. Using the mean value of h, the corrected bias becomes -8.8 mmHg.

We repeat the same procedure for the SDE, which is computed as follows

$$SDE = \sqrt{\frac{1}{n-1}\sum_{i=1}^{n}(I\hat{C}P_i + \rho g h_i - ICP_i - \frac{1}{n}\sum_{j=1}^{n}(I\hat{C}P_j + \rho g h_j - ICP_j))^2} =$$

$$\sqrt{\frac{1}{n-1}\sum_{i=1}^{n}(I\hat{C}P_i - ICP_i - \frac{1}{n}\sum_{j=1}^{n}(I\hat{C}P_j - ICP_j))^2 + \frac{1}{n-1}\sum_{i=1}^{n}(\rho g h_i - \frac{1}{n}\sum_{j=1}^{n}\rho g h_j)^2}$$

Using the same assumption for the distribution of h, we see that the variance of the contribution from the hydrostatic pressure is 10.1 mmHg. Correcting for this, we see that the corrected SDE is hardly changed at 14.7 mmHg. While the corrected bias is comparable to certain ICP measurement modalities, the SDE is still not acceptable. Furthermore, even with this correction, the TD approach still outperforms the SD approach. We attribute this to the sensitivities of the SD algorithm: the SD approach requires the spectrum of the input signal to be sufficiently rich and the approximation of CPP to be accurate. In contrast, the TD approach is more robust in the sense that the assumptions that it require are realizable with the richness of data obtained in current clinical practice.

In the next chapter, we elaborate on future explorations, both in regards to algorithmic development and data collection, to improve the SD approach.

4.3 Summary

In this chapter, we summarized the performance of the SD and TD algorithms on both a simulated and clinical dataset. In the simulated dataset, we found that the SD algorithm outperformed the TD algorithm, while in the clinical dataset, the performance of the TD algorithm surpassed the SD algorithm. We posit that the poor performance of the SD approach on clinical data is due to the fact that the measured waveforms are neither rich (in terms of the number of harmonics) nor accurate (in terms of morphology) enough to estimate ICP robustly. In the next chapter, we discuss future explorations to gain more insight into the cerebrovascular system.

Chapter 5

Conclusion and Future Work

This thesis presented a spectral density (SD) and a revised time-domain (TD) approach for intracranial pressure (ICP) estimation. In the first chapter, we describe the diagnostic value of ICP in a variety of pathologies that affect the brain and review the different measurement modalities, both invasive and non-invasive, used to measure ICP. In the second chapter, we reviewed the relevant background information required to develop our approach: the cerebrovascular physiology, the associated mathematical models, and the Kashif algorithm used to estimate ICP. We described the limitations of the algorithm that ultimately motivated our work. In the third chapter, we proposed two techniques to address the limitations of the Kashif algorithm. We proposed a heuristic to determine the time-offset parameter in the Kashif algorithm, and another ICP estimation algorithm based on the spectral density of the clinical waveforms. In the fourth chapter, we applied the algorithms to two datasets and analyze the performances.

5.1 Contributions

While the results of the SD-based algorithm for ICP estimation were not favorable, we nonetheless developed a novel approach that addressed the major limitations of using clinical data in model-based estimation. In summary, our key contributions are:

- The development of an estimation algorithm based on the spectral density of the input signals to first estimate the parameters of the cerebrovascular system and then ICP. In this approach, we sidestep the two major sensitivities of the Kashif algorithm, namely the determination of the time-offset parameter and the differentiation of real data.
- The understanding the sensitivities of the SD-based algorithm. By performing a systematic set of

simulation studies, we learned about the importance of signal quality in estimating ICP.

- The development of a new model of the cerebrovascular system, that incorporates the inertia of blood by the addition of an inductive element. Using this model, we were able to simulate realistic CBFV waveforms.
- The development of a heuristic for the determination of the time-offset parameter used in Kashif algorithm. Here, we proposed a heuristic that produced plausible ICP estimates that can serve as realistic lower bounds of the true ICP. Our work suggests that this heuristic is sufficient for pathologies where ICP remains low.

5.2 Future Work

The poor performance of the SD-based algorithm on archived data from patients with severe TBI motivates both algorithmic and experimental explorations to improve ICP estimation. We begin with a discussion of algorithmic explorations.

Algorithmic explorations In the SD-based algorithm, we observed that when the input signals were insufficiently rich, meaning that the number of harmonics in the signal spectrum is not sufficient for estimation, the resulting ICP estimates are poor. This motivates the exploration of algorithmic techniques to quantify the signal and the noise in the signal spectra. We describe two major considerations that we believe will improve ICP estimation. First, we propose developing a quantified metric that exploits the model structure to predict *a priori* if the signal quality of the input signals is sufficient for ICP estimation. Second, we propose developing quantified bounds based on the structured noise for the parameter estimates and consequently ICP. When ICP estimation is not possible, we hope to use the bounds on ICP to extract trends in signal.

Furthermore, in the SD-based algorithm, we observe that across a record, the ICP estimates can have substantial high-frequency noise. Here, we propose two possible branches of exploration. In the SD-algorithm, ICP is estimated independently from window to window. We propose the imposition of physiological constraints across the non-overlapping estimation windows. The addition of these constraints may reduce variability in the parameter estimates. Furthermore, in the SD-based approach, we are concerned with estimating the spectral density of the input signals. Currently, we are computing the FFT of segmented data, which introduces noise as a consequence of spectral leakage. Here, we propose applying different algorithms for spectral estimation that may minimize this noise.

Experimental explorations To accurately assess the performance of the SD-based algorithm, great care must be taken in data collection. Here, we stress the importance of measuring h, or the distance between the level of heart and the level of the cerebral arteries, as the resulting hydrostatic pressure is significant. Currently, in our error analysis, we observe that knowledge of this parameter will substantially lower the estimation bias.

In the SD-based algorithm, we approximate the morphology of the ABP waveform in the cerebral arteries to be the morphology of the ABP at the radial artery. We propose a series of explorations, both through clinical collaborations and animal experiments, to simultaneously measure the pressure waveforms in the cerebral circulation and the radial artery. One can then seek to develop an approximate transfer function to transform the measured peripheral ABP signal into the desired cerebral ABP signal. It is hoped that such a transformation will remedy the limitations of the measured ABP and allows the SD algorithm to estimate ICP on real data with the same high accuracy and precision as was achieved on the simulated data.

Appendix A: Discretization of Linear State Space Models

Here, we derive the discretization of continuous-time, linear state space models. Consider the following model

$$\dot{x}(t) = Ax(t) + Bu(t) \tag{5.1}$$

$$y(t) = Cx(t) + Du(t) \tag{5.2}$$

Solving for $x(t)$, we have

$$x(t) \quad = \quad x(0)e^{At} + \int_0^t e^{A(t-\tau)}Bu(\tau)d\tau \tag{5.3}$$

If we sample $x(t)$ every T seconds, we can rewrite (5.3) as

$$x[n] = x(nT) = x(0)e^{AnT} + \int_0^{nT} e^{A(nT-\tau)}Bu(\tau)d\tau \tag{5.4}$$

$$x[n+1] = x(0)e^{A(n+1)T} + \int_0^{(n+1)T} e^{A((n+1)T-\tau)}Bu(\tau)d\tau \tag{5.5}$$

Rearranging the terms of (5.5), we have

$$x[n+1] = x(0)e^{A(n+1)T} + \int_0^{nT} e^{A((n+1)T-\tau)}Bu(\tau)d\tau + \int_{nT}^{(n+1)T} e^{A((n+1)T-\tau)}Bu(\tau)d\tau \tag{5.6}$$

$$x[n+1] = e^{AT}\left(x(0)e^{AnT} + \int_0^{nT} e^{A(nT-\tau)}Bu(\tau)d\tau\right) + \int_{nT}^{(n+1)T} e^{A((n+1)T-\tau)}Bu(\tau)d\tau \tag{5.7}$$

$$x[n+1] = e^{AT}x[n] + \int_{nT}^{(n+1)T} e^{A((n+1)T-\tau)}Bu(\tau)d\tau \tag{5.8}$$

Here, we assume that $u(t)$ is sampled with zero-order hold. Denoting the sampled signal as $u[n]$, we have

$$\begin{aligned} x[n+1] &= e^{AT}x[n] + \int_{nT}^{(n+1)T} e^{A(n+1)T}e^{-A\tau}d\tau Bu[n] && (5.9) \\ x[n+1] &= e^{AT}x[n] + A^{-1}e^{A(n+1)T}\left\{e^{-AnT} - e^{-A(n+1)T}\right\}Bu[n] && (5.10) \\ x[n+1] &= e^{AT}x[n] + A^{-1}\left\{e^{AT} - I\right\}Bu[n] && (5.11) \end{aligned}$$

From (5.11), we see that (5.1) and (5.2) can be discretized as

$$x[n+1] = A_d x[n] + B_d u[n] \tag{5.12}$$

$$y[n] = Cx[n] + Du[n] \tag{5.13}$$

where $A_d = e^{AT}$ and $B_d = A^{-1}\{A_d - I\}B$. This concludes our derivation.

Appendix B: Using CBFV Instead of CBF in ICP Estimation

Here, we show that the use of cerebral blood flow velocity (CBFV) instead of cerebral blood flow (CBF) still allows for the correct estimation of ICP for all algorithms. Here, we denote CBFV as $\hat{q}(t)$. Without loss of generality, we consider the Kashif model

$$\hat{q}(t) = \frac{p(t) - ICP}{R} + C\frac{dp(t)}{dt} \tag{5.14}$$

Using the fact that CBFV and CBF are related by a scale factor, α, we have

$$q(t) = \frac{p(t) - ICP}{\alpha R} + \frac{C}{\alpha}\frac{dp(t)}{dt} \tag{5.15}$$

By using CBFV, the parameter estimates, which we denote as $\hat{R}$ and $\hat{C}$, we obtain are scaled by this multiplicative factor. We see that $\hat{R} = \frac{R}{\alpha}$ and $\hat{C} = \alpha C$. Furthermore, we see that ICP can be written as follows

$$ICP = MABP - \frac{R}{\alpha} \cdot MCBFV = MABP - R \cdot MCBF \tag{5.16}$$

where $MABP$, $MCBFV$, and $MCBF$ are the mean ABP, mean CBFV, and mean CBF, respectively.

Appendix C: Time-Offset Estimation Algorithm

The Kashif algorithm [11] requires the input signals to be physiologically aligned. Here, we discuss three algorithms, listed in order of preference, to determine the time-offsets used to shift the ABP waveform relative to the CBFV waveform.

Method 1 In [11], the cerebrovascular system is modeled by the following differential equation

$$q(t) \quad = \quad \frac{p(t) - ICP}{R} + C\frac{dp(t)}{dt} \tag{5.17}$$

where $p(t)$ and $q(t)$ are the ABP and CBFV waveforms, respectively; ICP is the mean ICP; and R and C are the aggregate resistance and capacitance of the cerebrovascular system. During the systolic upstroke, we can approximate (5.17) as

$$q(t) \quad \approx \quad C\frac{dp(t)}{dt} \tag{5.18}$$

In this approach, the ABP and CBFV waveforms are subdivided into non-overlapping windows that are comprised of 5 beats. For the i^{th} window, the time-offset τ_i is taken to be the time-offset such that when τ_i is applied to the windowed data, the peak flow velocity is maximally aligned with the maximum derivative of the ABP waveform. The time-offset for the entire record, τ, is equal to the median over all of the τ_i's.

Empirically, Kashif *et al.* found that when the ABP and CBFV waveforms were noise-free, this approach resulted in a time-offset parameter that minimized the error in ICP estimation. Next, we discuss an approximate algorithm to estimate τ when the ABP and CBFV are noisy.

Method 2 When $\frac{dp(t)}{dt}$ is minimized, (5.17) can be approximated as

$$q(t) \approx \frac{p(t) - ICP}{R} \tag{5.19}$$

In this approach, the ABP and CBFV waveforms are subdivided into non-overlapping windows that are comprised of 5 beats. For the i^{th} window, the time-offset τ_i is computed as

$$\tau_i = \arg\min_{\tau} \min_{ICP,R} \sum_{t \in T} |p(t+\tau) - ICP - Rq(t)|^2 + \frac{w}{2} \tag{5.20}$$

where T corresponds to points of where the ABP has low slope within the i^{th} window; and w is an equal to the average duration of the systolic upstroke. The time-offset for the entire record, τ, is equal to the median over all of the τ_i's.

Method 3 When $\frac{dp(t)}{dt}$ is minimized, (5.17) can be approximated as

$$q(t) \approx \frac{p(t) - ICP}{R} \tag{5.21}$$

In this approach, the ABP and CBFV waveforms are subdivided into non-overlapping windows that are comprised of 5 beats. For the i^{th} window, the time-offset τ_i is computed as

$$\tau_i = \arg\min_{\tau} \min_{ICP,R} \sum_{t \in T} |p(t+\tau) - ICP - Rq(t)|^2 \tag{5.22}$$

where T corresponds to points of where the ABP has low slope within the i^{th} window. The time-offset for the entire record, τ, is equal to the median over all of the τ_i's.

For all methods, if the applied time-offset results in ICP estimates that are negative for more than 10% of the record duration, the time-offset is incremented until that is no longer the case. Furthermore, Kashif discards candidate time-offsets when the variance over the corresponding τ_i's is too high. When the remaining candidate time-offsets do not agree, the ICP estimate is taken to be the average of the ICP estimates obtained by using the top two time-offsets, as determined by the algorithm preference.

Bibliography

[1] Facts about hydrocephalus. nhfonline.org/facts-about-hydrocephalus.htm, May 2014.

[2] Schematic diagrams of the anatomy of the brain. Wikipedia.org, May 2014.

[3] Stroke facts. www.cdc.gov/stroke/facts.htm, May 2014.

[4] Traumatic brain injury in the united states fact sheet. www.cdc.gov/traumaticbraininjury/, May 2014.

[5] CJ Avezaat, JH Van Eijndhoven, and DJ Wyper. Cerebrospinal fluid pulse pressure and intracranial volume-pressure relationships. *Journal of Neurology, Neurosurgery & Psychiatry*, 42(8):687–700, 1979.

[6] M Chacón, C Pardo, C Puppo, M Curilem, and J Landerretche. Non-invasive intracranial pressure estimation using support vector machine. In *Engineering in Medicine and Biology Society (EMBC), 2010 Annual International Conference of the IEEE*, pages 996–999. IEEE, 2010.

[7] Z Feldman, MJ Kanter, CS Robertson, CF Contant, C Hayes, MA Sheinberg, CA Villareal, RK Narayan, and RG Grossman. Effect of head elevation on intracranial pressure, cerebral perfusion pressure, and cerebral blood flow in head-injured patients. *Journal of Neurosurgery*, 76(2):207–211, 1992.

[8] X Hu, P Xu, S Wu, S Asgari, and M Bergsneider. A data mining framework for time series estimation. *Journal of Biomedical Informatics*, 43(2):190–199, 2010.

[9] ER Kandel, JH Schwartz, and TM Jessell. *Principles of neural science*, volume 4. McGraw-Hill New York, 2000.

[10] FM Kashif. *Modeling and estimation for non-invasive monitoring of intracranial pressure and cerebrovascular autoregulation.* PhD thesis, Massachusetts Institute of Technology, 2011.

[11] FM Kashif, GC Verghese, V Novak, M Czosnyka, and T Heldt. Model-based noninvasive estimation of intracranial pressure from cerebral blood flow velocity and arterial pressure. *Science Translational Medicine*, 4(129):129ra44–129ra44, 2012.

[12] ME Kerr, E Crago, and V Brotto. Nursing management: acute intracranial problems. *Lewis's Medical-Surgical Nursing: Assessment and Management of Clinical Problems*, pages 1493–1526, 2004.

[13] J Noraky, GC Verghese, DE Searls, V Lioutas, S Sonni, A Thomas, and T Heldt. Noninvasive intracranial pressure determination in patients with subarachnoid hemorrhage. In *15th International Conference on Intracranial Pressure and Brain Monitoring*, 2013.

[14] M O'Rourke, R Kelly, and A Avolio. *The Arterial Pulse.* Lea & Febiger, 1992.

[15] D Popovic, M Khoo, and S Lee. Noninvasive monitoring of intracranial pressure. *Recent Patents on Biomedical Engineering*, 2(3):165–179, 2009.

[16] A Ragauskas, V Matijosaitis, R Zakelis, K Petrikonis, D Rastenyte, I Piper, and G Daubaris. Clinical assessment of noninvasive intracranial pressure absolute value measurement method. *Neurology*, 78(21):1684–1691, 2012.

[17] R Sahni and J Weinberger. Management of intracerebral hemorrhage. *Vascular Health and Risk Management*, 3(5):701, 2007.

[18] B Schmidt, J Klingelhöfer, JJ Schwarze, D Sander, and I Wittich. Noninvasive prediction of intracranial pressure curves using transcranial doppler ultrasonography and blood pressure curves. *Stroke*, 28(12):2465–2472, 1997.

[19] DF Signorini. A clinical evaluation of the codman microsensor for intracranial pressure monitoring. *British Journal of Neurosurgery*, 12(3):223–227, 1998.

[20] LA Steiner and PJD Andrews. Monitoring the injured brain: Icp and cbf. *British Journal of Anaesthesia*, 97(1):26–38, 2006.

[21] M Ursino and CA Lodi. A simple mathematical model of the interaction between intracranial pressure and cerebral hemodynamics. *Journal of Applied Physiology*, 82(4):1256–1269, 1997.

[22] AR Zazulia, MN Diringer, CP Derdeyn, and WJ Powers. Progression of mass effect after intracerebral hemorrhage. *Stroke*, 30(6):1167–1173, 1999.

[23] W Zong, T Heldt, GB Moody, and RG Mark. An open-source algorithm to detect onset of arterial blood pressure pulses. In *Computers in Cardiology, 2003*, pages 259–262. IEEE, 2003.